Engineering Hibiscus-Like Riboflavin/ZIF-8 Microsphere Composites to Enhance Transepithelial Corneal Cross-Linking

Mei Yang, Wenjin Xu, Zhongxing Chen, Ming Chen, Xiaoyu Zhang, Huanhuan He, Yushan Wu, Xueyang Chen, Tianjiao Zhang, Mengdi Yan, Jieyi Bai, Colm McAlinden, Keith M. Meek, Jinjin Yu, Shengnan Ding, Rongrong Gao,* Jinhai Huang,* and Xingtao Zhou*

Riboflavin-5-phosphate (RF) is the most commonly used photosensitizer in corneal cross-linking (CXL), but its hydrophilicity and negative charge limit its penetration through the corneal epithelium into the stroma. To enhance the corneal permeability of RF and promote its efficacy in the treatment of keratoconus, novel hibiscus-like RF@ZIF-8 microsphere composites [6RF@ZIF-8 NF (nanoflake)] are prepared using ZIF-8 nanomaterials as carriers, which are characterized by their hydrophobicity, positive potential, biocompatibility, high loading capacities, and large surface areas. Both hematoxylin and eosin endothelial staining and TUNEL assays demonstrate excellent biocompatibility of 6RF@ZIF-8 NF. In in vivo studies, the 6RF@ZIF-8 NF displayed excellent corneal permeation, and outstanding transepithelial CXL (TE-CXL) efficacy, slightly better than the conventional CXL protocol. Furthermore, the special hibiscus-like structures of 6RF@ZIF-8 NF meant that it has better TE-CXL efficacy than that of 6RF@ZIF-8 NP (nanoparticles) due to the larger contact area with the epithelium and the shorter RF release passage. These results suggest that the 6RF@ZIF-8 NF are promising for transepithelial corneal cross-linking, avoiding the need for epithelial debridement.

1. Introduction

Keratoconus is a corneal disorder characterized by stromal thinning and ectasia, leading to irregular astigmatism and progressive visual loss.[1] Corneal cross-linking (CXL) can slow or even stop the progression of keratoconus and has been used for the treatment of some corneal diseases.[2,3] Riboflavin-5-phosphate (RF), a hydrophilic negatively charged molecule, is commonly used as a photosensitizer in CXL, while the corneal epithelium is hydrophobic and has a shell of negative potential protein on the surface that acts as a barrier for the passage of RF. The conventional CXL (C-CXL) protocol, as described by Wollensak, requires the debridement of the central 7–9 mm corneal epithelium, followed by the application of

M. Yang, Z. Chen, X. Zhang, C. McAlinden, J. Huang, X. Zhou
Eye Institute and Department of Ophthalmology
Eye and ENT Hospital
Fudan University
Key Laboratory of Myopia
Chinese Academy of Medical Sciences
Shanghai 200030, China
E-mail: jinhaihuang@fudan.edu.cn; xingtaozhou@fudan.edu.cn
M. Yang, Z. Chen, X. Zhang, J. Huang, X. Zhou
Shanghai Research Center of Ophthalmology and Optometry
Shanghai 200030, China
W. Xu, M. Chen, H. He, X. Chen, T. Zhang, M. Yan, J. Bai, J. Yu,
S. Ding, R. Gao
School of Ophthalmology and Optometry and Eye Hospital
Wenzhou Medical University
Wenzhou, Zhejiang 325027, China
E-mail: beargrr@163.com

Y. Wu
School of Power and Mechanical Engineering
Hubei International Scientific and Technological Cooperation
Base of Sustainable Resource and Energy
Wuhan University
Wuhan 430072, China
C. McAlinden
Department of Ophthalmology
Singleton Hospital
Swansea Bay University Health Board
Swansea SA2 8QA, UK
K. M. Meek
School of Optometry and Vision Sciences
Cardiff University
Cardiff CF24 4HQ, UK
K. M. Meek
Cardiff Institute for Tissue Engineering and Repair
School of Pharmacy and Pharmaceutical Sciences
Cardiff University
Redwood Building, King Edward VII Avenue, Cardiff CF10 3NB, UK

0.1% RF in 20% dextran to the deepithelialized cornea, and then continuous UVA irradiation (3 mW cm^{-2}) for 30 min with further RF solution applied every 5 min.[4] During this process, the RF in the corneal stroma is excited to a triplet state, which generates singlet oxygen and superoxide radicals and covalent bonding to stromal collagen fibers, resulting in inter and intra fibrillary cross links in the stromal lamellae. Thus, the bio-mechanical properties of cornea can be strengthened and its resistance to enzymatic digestion enhanced, which further prevents the thinning and deformation of the corneal profile, and subsequent deterioration in vision.[5–7] However, it is notable that the epithelium removal usually causes significant post-operative ocular pain and increases the risk of infectious keratitis. There may also be delayed healing or subsequent corneal edema and potentially scarring.[8,9] CXL protocols avoiding epithelial debridement [transepithelial corneal cross-linking (TE-CXL)] have been introduced to reduce the disadvantages associated with epithelial debridement.[10,11] Up to now, various methods have been explored, such as: infiltration enhancers,[12] vitamin E,[13] ion introduction,[14,15] ultrasonic introduction,[16] and partial de-epithelialization,[17] to improve the TE-CXL performance of the photosensitizer and increase the absorption of local RF. However, the concentration of RF in the corneal stroma is still lower than that of C-CXL or its distribution is uneven, which may weaken the efficacy of TE-CXL. Gore et al. used MedioCross TE, Ribocross TE, Paracel Plus VibeX Xtra, and Ricrolin+ ion transfer preparations. These are common commercial RF preparations currently used for TE-CXL in fresh cornea of isolated rabbit eyes, using 0.1% RF (VibeX Rapid, epithelium-off) infiltration as a positive control.[12] The peak concentration of RF in the most superficial corneal stroma (stromal depth 0–10 μm) was 0.09% (±0.01%) in the de-epithelialized control group, while the peak concentrations of RF MedioCross TE, Ricrolin+, Paracel/Xtra, and Ribocross TE were 0.054% (±0.01%), 0.031% (0.003%), 0.021% (±0.001%), and 0.015% (±0.004%), respectively. The concentration of RF decreased to be 0.075% (±0.006%) at a depth of 300 μm (the common demarcation area after CXL) in the de-epithelialized control group, which decreased to 0.018% (±0.006%) and 0.016% (0.002%) for the MedioCross and TE Ricrolin+ groups. The concentrations further decreased to be lower than 0.005% for the other groups. Other studies also verified that the content of RF in the corneal stroma after ion introduction was only about 50% of that of C-CXL.[14,15] Thus, controversy about the efficacy of TE-CXL RF preparations in clinical settings still exists, and about 1/3 to 1/2 of patients have disease progression after surgery. One of the main reasons is the insufficient RF content in the corneal stroma,[18] which may also increase the risks of tissue photo-damage during UVA irradiation.[19,20] In addition, the above methods require physical or chemical modification of the corneal tissue, which still has the risk of corneal injury.[17] Thus, it is of great importance to find a material that can deliver hydrophilic RF to permeate the hydrophobic corneal epithelium and reach the corneal stroma at high concentration.

Nanomaterials such as polymeric nanoparticles and inorganic nanoparticles have also been developed to deliver RF to the corneal stroma.[21–24] As a class of hydrophobic materials, porous metal–organic frameworks (MOFs), especially nanosized MOF, has received much attention in recent years.[25–27]

These are hybrid materials formed by self-assembly of polydentate bridging ligands and metal-connecting points, and can be obtained under relatively mild conditions as either crystalline or amorphous material. The size, composition and morphology of the obtained MOF can be tuned by adjusting the synthesis conditions. The special physicochemical features including structural and chemical diversity, high surface areas and loading capacities, tailorable pore sizes, good biocompatibility, and biodegradability, give them some potential advantages over conventional nanomedicines, and make them excellent candidates to act as drug carriers.[28–30] MOFs can solve the difficult control of inorganic carrier release and the low loading capacity of organic carriers. They can control the drug release rate preventing the blood drug concentrations getting too high and avoiding frequent fluctuations of blood drug concentration, and they can allow drugs to remain above the effective concentration for longer time intervals. Besides, MOF composites can be further modified with other agents to improve stability, fine-tune properties, and impart additional functionality. Up to now, various nanosized MOFs used to deliver anticancer drugs and other chemotherapeutics showed a sustained drug release, and in vitro assays revealed that the nanoencapsulated drug possessed similar efficacy to the free drug.[31,32] Although still at a very early stage of development, nanosized MOFs have already shown great promise as a novel platform for nanomedicine. The compositional stability and mild synthetic conditions allow them to incorporate other agents, and to deliver their cargo effectively to targeted cells in vivo.[33]

As a subclass of MOFs, zeolitic imidazolate frameworks (ZIFs), especially nanosized ZIF-8 which is prepared using zinc ions and 2-methylimidazolate as raw materials, have been widely used as carriers for many drugs.[34–38] The positive potential of ZIF-8 also can counteract the negative potential of the corneal epithelium, and their similar hydrophobicity facilitates the passage of the ZIF-8 through the epithelium.

With this purpose, novel hibiscus-like RF@ZIF-8 microsphere composites (6RF@ZIF-8 NF) were synthesized using the one-pot method (**Scheme 1**). Their TE-CXL effects were evaluated in detail in this paper and the results indicated that 6RF@ZIF-8 NF had a better TE-CXL effect than C-CXL, as indicated by the darker green color in the slit lamp photos, confocal fluorescence images with higher intensity, similar enzymatic digestion time of the constituent collagen, and higher stress-strain intensity.

2. Results and Discussion

2.1. Material Characterization of ZIF-8 and RF@ZIF-8 Composites

Initially, scanning electron microscopy (SEM) and transmission electron microscopy (TEM) of ZIF-8 NP, ZIF-8 NF, and 6RF@ZIF-8 NF were carried out. As shown in **Figure 1**, ZIF-8 NP were mainly composed of nanoparticles with size ≈50–70 nm; SEM imaging indicated that the nanoparticles were polyhedrons with smooth surfaces; and TEM images confirmed the polyhedron structure as well showing the porous structure of the sample. When the concentration of Zn(NO$_3$)$_2$ and 2-mim in the original solution was decreased to 1/4 of that of ZIF-8
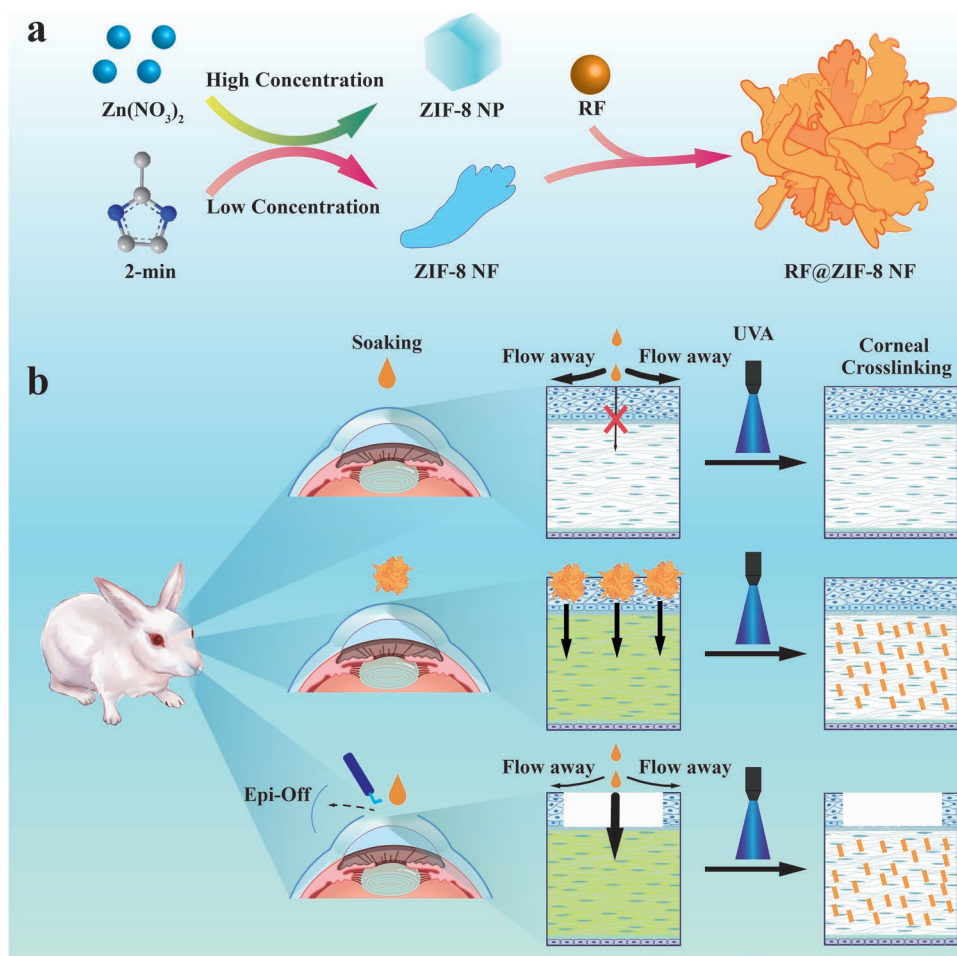
Scheme 1. a) The synthesis of RF@ZIF-8 composites and b) CXL application.

NP, ZIF-8 NF was obtained. Compared with ZIF-8 NP, the size of the ZIF-8 NF decreased dramatically as seen in the SEM; TEM images indicated that the product consisted of irregular nanoflakes with the porous property maintained. Interestingly, the addition of RF in the reaction solution can influence the morphology of the final RF@ZIF-8 composites, especially the sample obtained in 6 mg mL^{-1} RF solution, which displayed a hibiscus-like microsphere composed of nanoflakes that tended to adhere to each other.

The phase structures of the ZIF-8 nanomaterials obtained at different Zn(NO$_3$)$_2$ and 2-mim concentration, and the influence of the doping amounts of RF on the phase structure of the RF@ZIF-8 composites were investigated through measurement of XRD patterns. As shown in **Figure 2**a, for the ZIF-8 nanomaterials without RF doping, all diffraction peaks were the same as the simulated ZIF-8; no other diffraction peaks could be observed, indicating a successful synthesis of ZIF-8. Meanwhile, the different intensity of the diffraction peaks may be ascribed to a change of the morphology that likely influences the perfection of the ZIF-8 crystal structure. When different amounts of RF were added to the ZIF-8 NF raw material reaction solution, the intensity of the diffraction peaks from the RF@ZIF-8 composites clearly decreased when the

RF concentrations were increased. When the concentration of RF increased to 8 mg mL^{-1}, several main diffraction peaks before 20° ascribed to ZIF-8 disappeared. This suggests that the loading of RF in the RF@ZIF-8 composites could influence the crystal structure of ZIF-8, which may be ascribed to the presence of RF that has a strong coordination ability to the Zn^{2+} ions of ZIF-8 and the decrease of the ratio of ZIF-8 to RF.

Meanwhile, the composition of the ZIF-8 NP, ZIF-8 NF, and hibiscus-like 6RF@ZIF-8 NF were further compared with the purpose to find the interaction among different elements. Seven elements including C, N, H, Zn, P, O, and Na were measured using ICP-MS analysis (P, Zn, Na) and elements analysis (C, H, O, N). The obtained results were shown in Figure 2b with O elements content as reference value, which is not accurate due to the existence of O$_2$ in air. Comparing with ZIF-8 NP and ZIF-8 NF, elements Na and P can only be found in the samples of 6RF@ZIF-8 NF, indicating the successful loading of RF in ZIF-8 NF. It can also be found that the relative content of Zn, N, C, and H elements in 6RF@ZIF-8 NF are lower than that in other two samples ascribed to the existence of RF(C$_{17}$H$_{20}$N$_4$NaO$_9$P). Comparing the element content percentage of ZIF-8 NP and ZIF-8 NF (C, H, Zn, N), slightly lower of C, Zn content and similar H, N content can be
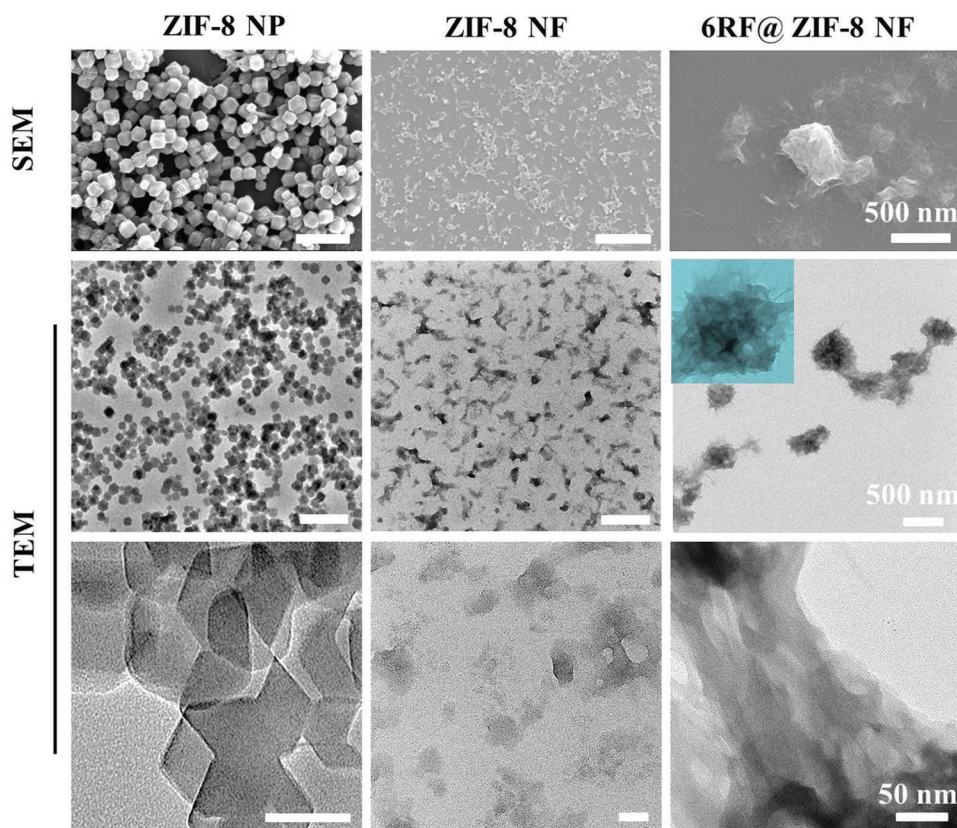
Figure 1. SEM and TEM imaging of ZIF-8 NP, ZIF-8 NF, and hibiscus-like 6RF@ZIF-8 NF.

observed in ZIF-8 NF. Combining the relatively higher O element content in ZIF-8 NF and its special morphology, the lower content percentage of C and Zn may be ascribed to the higher absorption quality of O_2 in the sample, while the nanoflake morphology of ZIF-8 NF may consume more 2-mim as part N atoms do not form coordination bonds with Zn atoms, resulting in the similar H and N content (details can be found Figure 4).

The FT-IR spectra of the ZIF-8 NP, ZIF-8 NF, RF, RF@ZIF-8 composites obtained at different RF concentrations are shown in Figure 2c. It was found that the peak position of ZIF-8 NP was the same as that of ZIF-8 NF, indicating that the same chemical bonds existed in both samples, and the variation of morphology had little effect on the formation of chemical bonds. The characteristic peaks of ZIF-8 could be observed in the spectra, such as the peak at 3126 cm^{-1}, attributed to the C−H stretching of imidazole. The peak located at 1630 cm^{-1} was attributed to the C-N stretching, with peaks in the range of 900–1350 cm^{-1} ascribed to the in-plane bending of the imidazole ring, while the peaks below 800 cm^{-1} were due to the out-of-plane bending of imidazole.[39,40] When RF was added to the reaction solution, the FT-IR spectra of the obtained RF@ZIF-8 composites were similar with that of ZIF-8 nanomaterials except that several absorption bands ascribed to RF could be observed. The characteristic peaks ascribed to ZIF-8 could still be observed, which were further confirmed by the XPS spectra.

The XPS spectra of the 6RF@ZIF-8 NF are shown in Figure 2d–f and Figure S1, Supporting Information. The

spin-orbit split of C, N, O, P, and Zn elements could be observed in the survey scan spectra (Figure 2d). For the detailed scan of C spectra (Figure S1a, Supporting Information), in addition to the sp^2- bonded carbon C−C at 284.5 eV, the peaks at 285.6 eV, 288 eV were assigned to the C1s of the C−OH, C=O groups, respectively. For the O1s XPS data (Figure 2e), the peak located at 530.2 eV could be ascribed to the O−Zn bonds, indicating the newly formed coordination bond in 6RF@ZIF-8 NF. The peak at 531.7 eV could be attributed to C=O bond,[41,42] while the weak peak located at 535 eV could be attributed to covalent oxygen, such as P−O bonds of RF, and surface H_2O, CO_2.[43] Three weak peaks located at 398, 398.6, and 400 eV were observed in the N1s XPS spectra (Figure 2f). The peak at 398 eV could be attributed to the N−Zn bond, indicating the coordination bond between Zn and imidazole remained in the new composites, the peak at 398.6 eV could be attributed to the N−H bond, while the peak located at 400 eV should be due to the C−NH groups of imidazole and RF. Three peaks located at 131.98, 132.85, and 139.29 eV were also observed in the P XPS spectra (Figure S1b, Supporting Information). Among them, the peak at 131.98 eV should be due to the P $2p_{3/2}$, while the peak located at 132.85 eV should be ascribed to P $2p_{1/2}$, the other peak at 139.29 eV should be due to the Zn 3s or the newly formed P−Zn bonds. For the XPS spectra of Zn (Figure S1c, Supporting Information), two peaks at 1020.5 and 1043 eV were observed; the peak at 1020.5 eV was ascribed to the Zn $2p_{3/2}$, while the peak at 1043 eV should be assigned to Zn $2p_{1/2}$. These results were further confirmed by the density functional theory
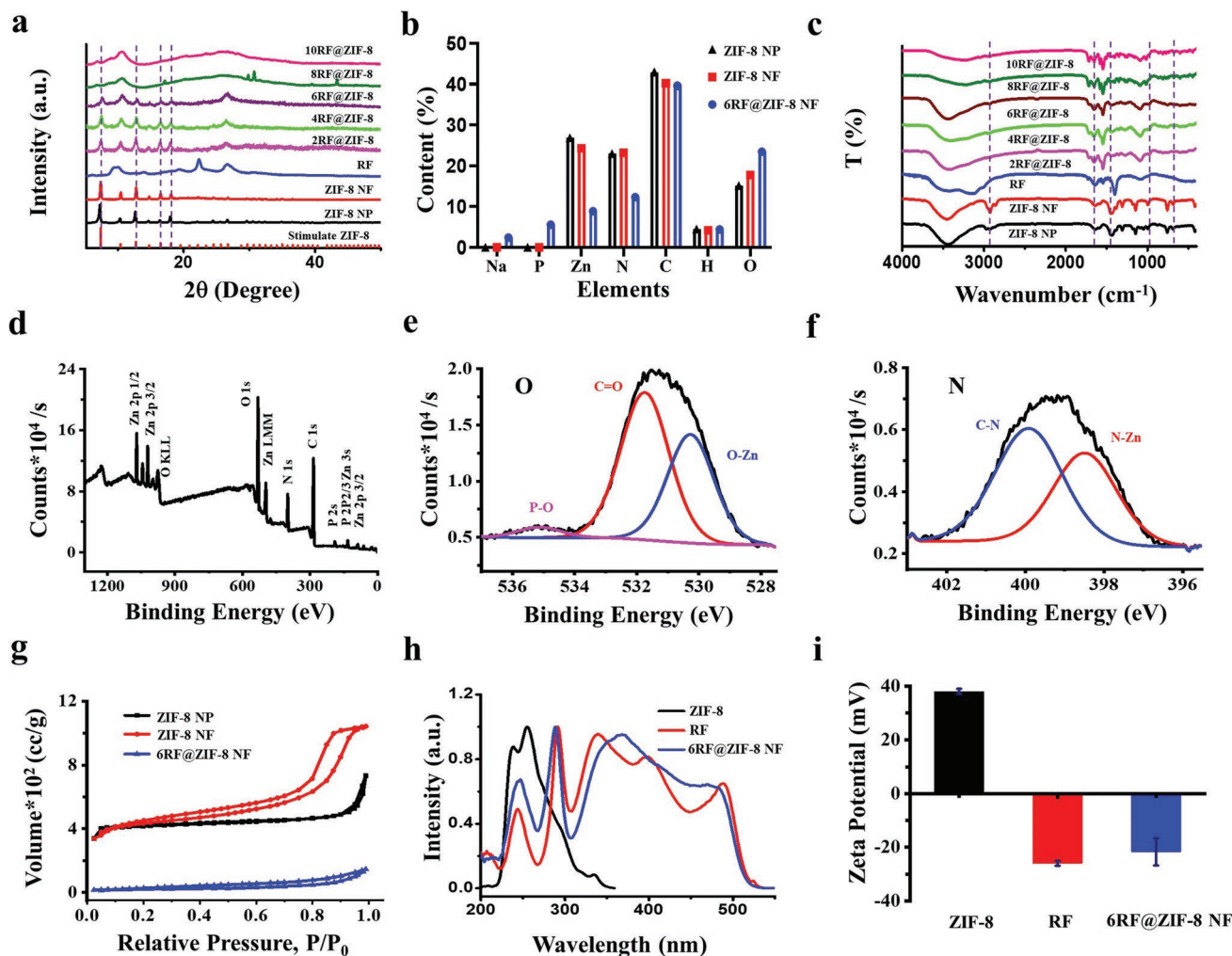
Figure 2. a) The XRD patterns of ZIF-8 NP, ZIF-8 NF, RF as well as RF@ZIF-8 composites obtained at different RF concentrations. b) The composites of ZIF-8 NP, ZIF-8 NF, and 6RF@ZIF-8 NF using ICP-MS analysis (P, Zn, Na), and elements analysis (C, H, O, N). c) FTIR of ZIF-8 NP, ZIF-8 NF, RF as well as RF@ZIF-8 composites with different concentration. d–f) XPS spectra of 6RF@ZIF-8 NF. g) N_2 gas adsorption/desorption analysis of ZIF-8 NP, ZIF-8 NF, and 6RF@ZIF-8 NF. h) Excitation spectra of ZIF-8, RF and 6RF@ZIF-8 NF composites. i) The zeta potential of ZIF-8, RF and 6RF@ZIF-8 NF (deionized water, pH = 7, $n \geq 3$).

(DFT) which was used to simulate the RF/ZIF-8 composites (**Figure 3**c–h).

An important property of an excellent carrier is possessing a large Brunauer–Emmett–Teller (BET) surface area. Thus, the N_2 gas adsorption/desorption analysis of the obtained ZIF-8 NP, ZIF-8 NF as well as 6RF@ZIF-8 NF was carried out to characterize the surface area and porosity of the samples. As shown in Figure 2g, the adsorption/desorption isotherm of these curves had features of types I and IV with a wide range of porosity varying from micropores to mesopores. The BET surface area of ZIF-8 NP was 1336.48 m^2g^{-1} with a pore diameter of ≈1.19 nm, when the amounts of raw materials decreased to be 1/4 of that of ZIF-8 NP; the BET surface area of ZIF-8 NF was 1163.74 m^2g^{-1} with pore diameter about 1.353 nm, compared with the curve of ZIF-8 NP. The appearance of a hysteresis loop further confirmed the changes of the pore distribution. On the basis of the SEM and TEM images of two samples, the changes of the BET surface area curves and the appearance of a

hysteresis loop should be due to the morphology variation from NP to NF, which made the pore develop higher permeability. When RF was added to the ZIF-8 NF raw material solution to synthesize 6RF@ZIF-8 NF, the BET surface area decreased to 75.08 m^2g^{-1} with a pore diameter of 1.19 nm, much lower than that of ZIF-8 NF, indicating successful loading of RF. Along with the SEM and TEM imaging of the two samples, it appears that the increase of the size can also reduce the BET value of 6RF@ZIF-8 NF due to the formation of the microspheres.

It is known that continuous UVA of 365 nm wavelength is usually used for CXL, this can excite RF into a triplet state and generate singlet oxygen and superoxide radicals. Therefore, it is of great interest to study the mutual effect of ZIF-8 and RF on the luminescence properties of 6RF@ZIF-8 composites. Thus, the variation of excitation and emission spectra of ZIF-8 NP, RF, and 6RF@ZIF-8 composites in aqueous solution were characterized. As shown in Figure 2h and Figures S2, S3, Supporting Information, monitoring at 370 nm, two excitation
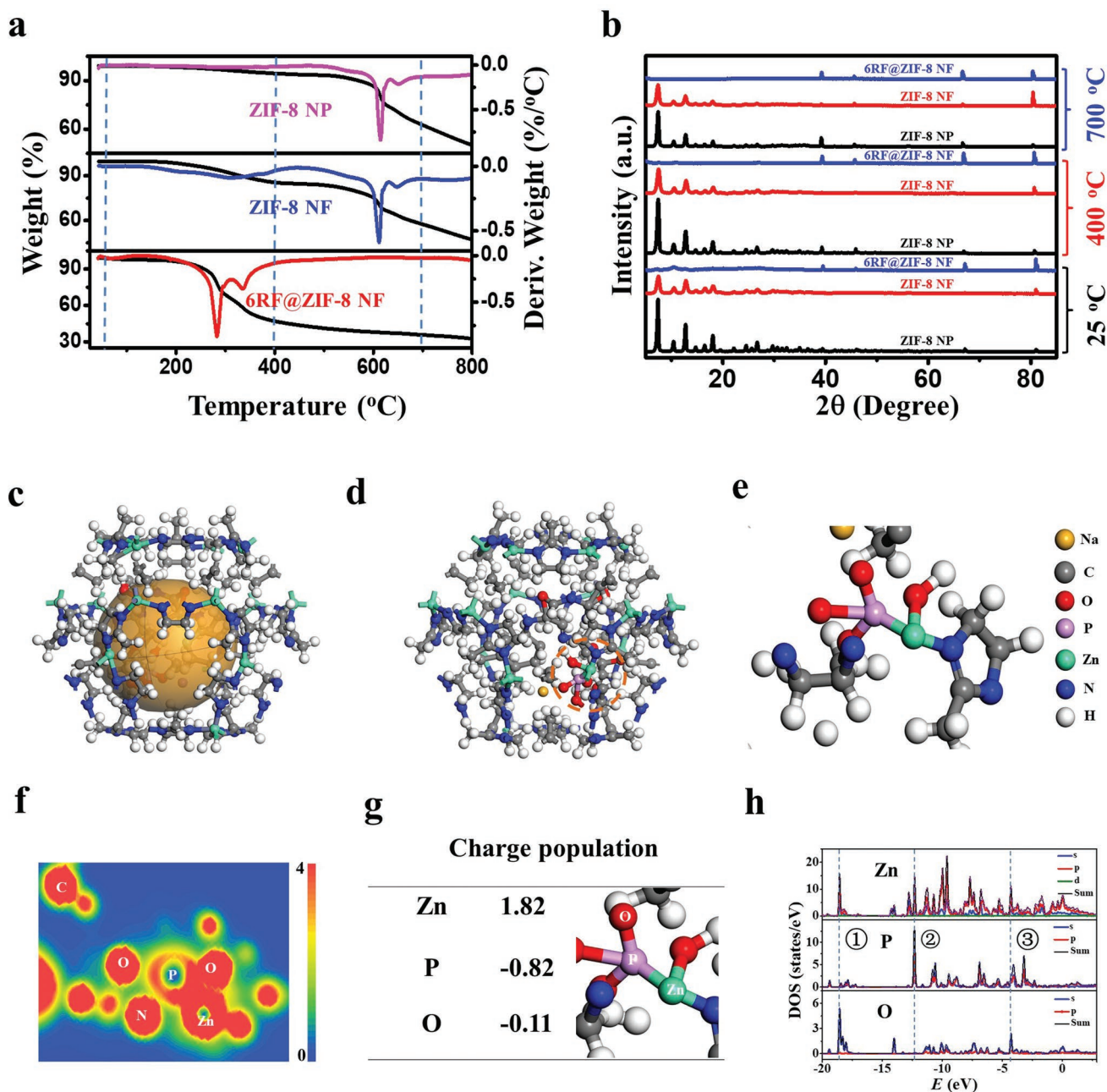
Figure 3. a) TG-DSC curves of ZIF-8 NP, ZIF-8 NF, and 6RF@ZIF-8 NF. TG curves shown in black. b) High temperature XRD of ZIF-8 NP, ZIF-8 NF, and 6RF@ZIF-8 NF. c–e) Model schematic diagram of RF/ZIF-8 composite, in which orange, dark grey, red, purple, green, blue and hoary spheres represent Na, C, O, P, Zn, N, and H atoms respectively. f,g) Charge density distribution of P, Zn, O, N, and C systems, where + and − represent gained and lost electrons respectively. h) PDOS diagram of O, P, and Zn for RF/ZIF-8 system.

bands located at 254 and 336 nm could be observed for ZIF-8 NF. Under excitation of 254 nm, three emission bands located at 320, 360, and 625 nm were found (Figure 2h). While for RF and 6RF@ZIF-8 NF aqueous solution, it can be seen that the concentration of RF has a dramatic influence on the excitation spectra under monitoring at 530 nm (Figure S2a,c, Supporting Information); the number of the excitation bands increased with the decrease of RF concentration in the solution, and the band located around 365 nm appeared when the concentration decreased to 0.325 mg mL^{-1}. Under excitation at 365 nm

(the wavelength for CXL), strong emission bands around 530 nm were found for RF and 6RF@ZIF-8 NF (Figure S2b,d, Supporting Information). The normalized excitation and emission spectra of RF and 6RF@ZIF-8 NF with an RF concentration of 0.325 mg mL^{-1} are shown in Figures 2h and Figure S3a, Supporting Information. Comparison with the excitation spectrum of RF reveals a different relative intensity and location of the maximum peaks of 6RF@ZIF-8 NF, which may be ascribed to the existence of ZIF-8 (Figure 2h). Meanwhile, it can be seen that there is no difference in the emission spectra of RF
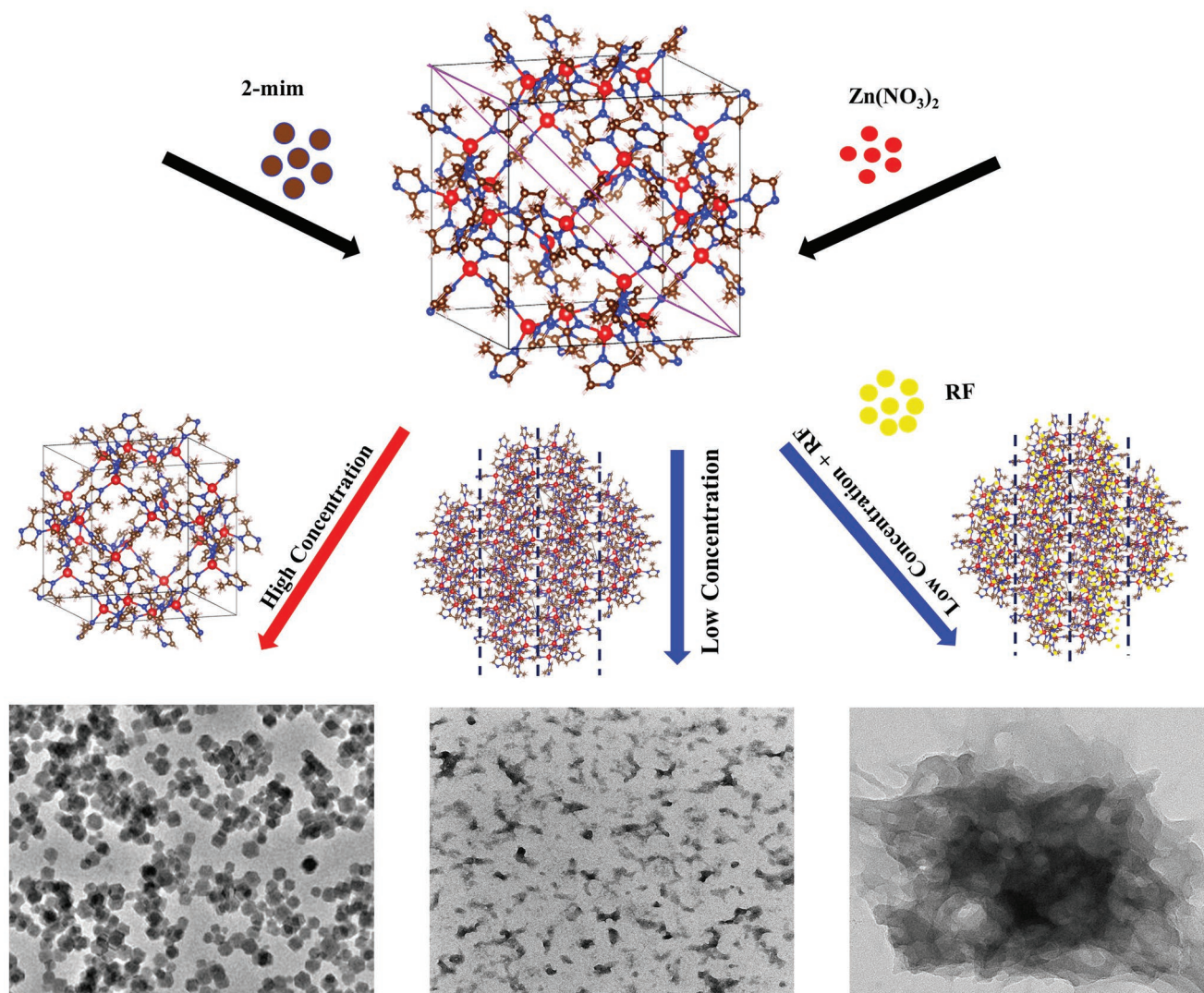
Figure 4. The formation scheme of the ZIF-8 NP, ZIF-8 NF, and 6RF@ZIF-8 NF.

and 6RF@ZIF-8 NF aqueous solution (Figure S3a, Supporting Information, due to overlap, the emission spectrum of RF was shown in Figure S3b, Supporting Information). This should be ascribed to the hydrophilia of RF, especially in aqueous solution at low concentration, which can quickly escape from ZIF-8, resulting in the similarity of the emission spectra of RF and 6RF@ZIF-8 NF in aqueous solution. Considering the micro-solubility of RF in ethanol and the stability of ZIF-8, RF can stay in ZIF-8 composites if 6RF@ZIF-8 NF is dispersed in ethanol. The influence of the solvent on the excitation and emission spectra of the 6RF@ZIF-8 NF were further studied, as shown in Figure S4, Supporting Information, for the same RF concentration (0.325 mg mL^{-1}), and the intensities of the excitation and emission spectra of 6RF@ZIF-8 NF in ethanol solution were found to be higher than in aqueous solution. Besides, under the same excitation at 365 nm, one emission band located at 555 nm can be observed in the composite in ethanol solution, rather than at 530 nm in the composite in aqueous solution, an obvious redshift for 6RF@ZIF-8 NF ethanol solution. Meanwhile, one emission band around 420 nm also can

be observed. These results further confirmed the influence of ZIF-8 on the luminescent properties of 6RF@ZIF-8 NF, and there should be some energy transfer between ZIF-8 and RF.

Moreover, the zeta potentials of the ZIF-8 nanomaterials, RF, and RF@ZIF-8 composites in deionized water with pH about 7 obtained under different conditions were compared, and the results are shown in Figures 2i and Figure S5, Supporting Information. It was found that the zeta potential of ZIF-8 nanomaterials was ≈40 mV, while RF had an opposite potential, about −25 mV. The experimental results demonstrated that the zeta potential of 6RF@ZIF-8 NF was also negative (−21 mV), a little higher than RF. The hydrophilic properties of RF mean that it can easily escape from the composites and exist in the solution, resulting in the lower measured value of zeta potential of RF@ZIF-8 composites. Meanwhile, the influence of the RF concentration and ZIF-8 raw material concentration in the initial reaction solution on the zeta potential of the final RF@ZIF-8 composites was also studied. As shown in Figure S5, Supporting Information, it was found that for the same concentration of Zn(NO$_3$)$_2$ and 2-mim, the zeta potential of the

2109865 (7 of 17)

**ADVANCED
SCIENCE NEWS**

www.advancedsciencenews.com

**ADVANCED
MATERIALS**

www.advmat.de

composites solution decreased with the enhancement of RF concentration. The zeta potential decreased from −16.5 ± 4.60 to −22.9 ± 2.5 mV when the RF concentration increased from 2 to 6 mg mL^{-1} (Figure S5a, Supporting Information). Further increasing RF concentration resulted in relatively small changes of the zeta potential, which may be due to the saturation of RF in aqueous solution. On the contrary, if the RF concentration in the reaction solution was fixed (6 mg mL^{-1}), the zeta potential of the final RF@ZIF-8 composites increased with the enhancement of Zn(NO$_3$)$_2$ and 2-mim concentration (Figure S5b, Supporting Information). The zeta potential increased from −21.7 ± 5.11 to −14.2 ± 7.13 mV when the ratio of Zn(NO$_3$)$_2$ and 2-mim concentration increased from 1/4 concentration of ZIF-8 NP to that of ZIF-8 NP. All of these results indicated that the final zeta potential of the composites was decided by the relative ratio of ZIF-8 raw materials (Zn(NO$_3$)$_2$ and 2-mim) to RF.

2.2. Formation Mechanism of 6RF@ZIF-8 NF

In order to study the possible formation mechanism of hibiscus-like 6RF@ZIF-8 NF, the influence of reaction time as well as the concentration of RF in the reaction solution was initially studied. As shown in Figures S6 and S7, Supporting Information, only microflakes were observed when the reaction time was controlled at 1 h (Figure S6, Supporting Information 1 h). The size of microflakes increased when the reaction time was prolonged to 2 h, and the microflakes tended to connect with each other (Figure S6, Supporting Information 2 h). When the reaction time was increased to 3 h, the accumulation of microflakes became more complex, and simple hibiscus-like microspheres composites could be observed (Figure S6, Supporting Information 3 h). When the reaction time was longer than 4 h, larger hibiscus-like microsphere composites were obtained (Figure S6, Supporting Information 4 h).

Next, the influence of RF concentration on the morphology of the final products was studied. The RF concentrations in the initial solution were controlled at 0, 2, 4, 6, 8, and 10 mg mL^{-1}, and the SEM images of the obtained RF@ZIF-8 composites showed that the addition of RF could affect the morphology of the composites dramatically (Figure S7, Supporting Information). Only ZIF-8 NF was obtained when there was no RF added (Figure S7, Supporting Information, 0 mg mL^{-1}). When the RF concentration in the reaction solution was 2 mg mL^{-1}, the morphology of RF@ZIF-8 composites changed to be nanoparticles with lots of glutinous substance coexisting with them (Figure S7, Supporting Information, 2 mg mL^{-1}). Further increasing the RF concentration to 4 mg mL^{-1}, the size of the nanoparticles increased and the agglomeration became more complex (Figure S7, Supporting Information, 4 mg mL^{-1}). When the RF concentration was increased to 6 mg mL^{-1} (Figure S7, Supporting Information, 6 mg mL^{-1}), the hibiscus-like microsphere composite, composed of flake petals adhered to each other, was formed. Further increasing the concentration of RF to 8 mg mL^{-1}, yielded composites mainly composed of nanoflakes (Figure S7, Supporting Information, 8 mg mL^{-1}). When the concentration of RF was increased to 10 mg mL^{-1}, the morphology changed back to nanoparticles connected with floccule (Figure S7, Supporting Information, 10 mg mL^{-1}). These results

indicated that the concentration of RF in the reaction solution dramatically influences the final morphology. Taking the RF solubleness in ethanol into consideration, we believe that when the concentration of RF was controlled, it tended to link ZIF-8 NF together, while nanoflakes or nanoparticles appeared again when the concentration of RF was too high, as the undissolved RF may be used as a seed to produce nanoparticles.

Vice versa, when the RF concentration in the reaction solution (taking 6 mg mL^{-1} RF concentration as an example) was fixed, increasing the Zn(NO$_3$)$_2$ and 2-mim concentration in the reaction solution also affected the final morphology of the composites. As shown in Figure S8, Supporting Information, the morphology of the composites varied from the initial hibiscus-like microsphere (6RF@ZIF-8 NF) to nanoparticles with the increase of Zn(NO$_3$)$_2$ and 2-mim concentration (Figure S8, Supporting Information, 1/4-4/4). Besides, with increased amounts of ZIF-8 raw materials, the size of the nanoparticles increased correspondingly, and the linkage between nanoparticles decreased gradually. When the concentration of zinc nitrate and 2-mim increased to that of ZIF-8 NP (240 mg Zn(NO$_3$)$_2$ and 480 mg 2-mim), monodispersed RF@ZIF-8 nanoparticles (6RF@ZIF-8 NP) with a size of ≈130 nm and with a rough surface were obtained (Figure S8, Supporting Information, 4/4). These were much larger than pure ZIF-8 NP (Figure 1a, 50–70 nm), indicating that the addition of RF in the reaction solution could enlarge the size and influence the final morphology of the composites.

In order to further study the possible interaction between RF and ZIF-8, as well as the effect of RF on ZIF-8 crystals, thermogravimetry (TG) and differential scanning calorimetry (DSC) were caried out to measure the thermal response of ZIF-8 NP, ZIF-8 NF and 6RF@ZIF-8 NF and then high-temperature XRD and theory simulation of the RF/ZIF-8 composites were executed to examine the effects of temperature on the crystal structures. TG-DSC curves from ZIF-8 NP, ZIF-8 NF and 6RF@ZIF-8 NF are shown in Figure 3a. It can be seen that that the DSC and TG curves of ZIF-8 NP and ZIF-8 NF were similar, except that one more endothermic peak was found in the range 150—400 °C in the DSC of ZIF-8NF together with a slightly different weight loss ratio in the TG curve; this indicates that there should be something different between ZIF-8 NP and ZIF-8NF. The addition of RF in the ZIF-8 system made the TG-DSC curves change dramatically, the location of the endothermic peak decreased from 600 to 270 °C in DSC and the temperature at which the main weight loss took place decreased from 600 to 270 °C in the TG curve, indicating a change in the crystal structure. A series of temperatures between 25 and 700 °C was then chosen to execute the high temperature XRD of ZIF-8 NP, ZIF-8 NF, and 6RF@ZIF-8 NF, and the results are shown in Figure S9, Supporting Information and Figure 3b. For the three samples, the intensity of the diffraction peaks increased with temperature to a certain degree, and then decreased again (Figure S9, Supporting Information). For 6RF@ZIF-8 NF, the diffraction peaks located below 30 ° disappeared when the temperature was >500 °C (Figure S9c, Supporting Information). These results indicated that the treatment temperature can influence the crystal structure of the three samples. Then, the XRD patterns of the three samples at 25, 400, and 700 °C were further compared

**ADVANCED
SCIENCE NEWS**

www.advancedsciencenews.com

**ADVANCED
MATERIALS**

www.advmat.de

(Figure 3b). The diffraction peaks of ZIF-8 NF and ZIF-8 NP were present throughout the heating process, indicating that the crystal structure of ZIF-8 remained. The diffraction peak intensity of ZIF-8 NP was the strongest of the three samples, and that of 6RF@ZIF-8 NF was weakest. Furthermore, the diffraction peak at 80.5° increased with temperature more in ZIF-8 NF than in ZIF-8 NP. Comparing 6RF@ZIF-8 NF with ZIF-8 NF, the diffraction peaks at 39, 45, and 66° increased dramatically with increasing temperature. All of these results demonstrate the different effects of temperature on structure between the three samples. The morphology change and the doping of RF can influence some crystal faces of ZIF-8 by the absence or formation of coordination bonds.

To study the interaction between RF and ZIF-8 more exactly, density functional theory (DFT) was further used to simulate the RF/ZIF-8 composites using the CASTEP module of Materials Studio. The supercell lattice length was 17 Å, the group space was 1 P1 and the angle $\alpha, \beta, \gamma = 90°$. The RF molecule whose structure is shown in Figure S10, Supporting Information, was placed at the center of the supercell. The calculation results showed that the optimized ZIF-8 model could adsorb RF molecules. Therefore, this model was further used to conduct first-principle calculations. In order to obtain the charge density and total energy, we used the generalized gradient approximation (GGA) with the Perdew—Burke–Ernzerhof (PBE) function to calculate the exchange potential and the correlation potential. The energy cutoff was set to be 450 eV. The convergence standard was 10^{-6} eV atom^{-1}, and the maximum force is <0.002 eV Å^{-1}.

The calculation indicated that in the optimized model, RF molecules can be wrapped in ZIF-8 cells by forming new bonds, such as P-Zn, O-Zn bonds, (Figure 3c–e). The distribution of the electron cloud in real space, which corresponds to the geometric structure in Figure 3e, further confirms the formation of the new bonds (Figure 3f). The electron clouds of the P atom with the Zn atoms have an electron cloud overlap, indicating that P atoms form bonds with the Zn atoms. Similar phenomena could also be observed between O atoms and Zn atoms; this indicates the transfer of electrons from Zn atoms to O and P atoms, and the existence of P—Zn, O—Zn bonds (Figure 3g). The partial densities of states (PDOS) for O, P and Zn in Figure 3h further confirmed the interaction between RF and ZIF-8. The Zn-p orbital resonated with the O-s orbital at some peak positions (line ① and line ③), proving that hybridization between the Zn—p orbital and the O-s orbital occurred and the formation of O—Zn bond. Similar phenomena also can be found between Zn—p orbital and the P-p orbital (line ②), indicating the formation of P—Zn bond. These results further verified the XPS results (Figure 2d and Figure S1b, Supporting Information).

Based on the above information, it can be concluded that the raw material concentration of ZIF-8 (Zn(NO₃)₂ and 2-mim) and the RF concentration in the initial reaction solution could affect the final morphology of RF@ZIF-8 composites, and the formation of the hibiscus-like microsphere composites should thus depend on the ZIF-8 crystal structure and the addition of RF. As shown in **Figure 4**, like many reports in the literature, the ZIF-8 crystal structure can induce the formation of ZIF-8 micro/nanoparticles when the Zn(NO₃)₂ and 2-mim concentration is

increased until there are enough raw materials present to make the crystal structure grow perfectly.[44,45] When the Zn(NO₃)₂ and 2-mim concentration was very low, only irregular ZIF-8 NF was obtained, which may be ascribed to the raw material being used up at the initial reaction stage, resulting in the imperfection of crystal structure. Meanwhile, a molecular layer of 2-mim can be observed diagonally in the crystal structure (indicating using purple lines), which separate the Zn-2-mim cluster into layers and may tend to lead to the formation of irregular nanoflakes if there are no Zn atoms linked on the other N atoms of 2-mim ligand rings. Besides, it is known that the presence of -PO₄³⁻ in the RF could lead to the formation of coordination bonds with the Zn²⁺ ions of ZIF-8, such as P—Zn, O—Zn bonds. Thus, the existence of RF can link nanoflakes together to form agglomerates through coordination bonds, and further influence the final morphology of RF@ZIF-8 composites (Figure S7, Supporting Information, 0–10 mg mL⁻¹). Thus, hibiscus-like 6RF@ZIF-8 NF microsphere composites could be obtained with the addition of RF; the formation of the complex surface of the 6RF@ZIF-8 NP (Figure S8, Supporting Information, 4/4) further confirmed this speculation.

2.3. Evaluation of Corneal RF Absorption Using RF@ZIF-8 Composites

Corneal RF absorption experiments were carried out and the distribution of RF in the cornea was studied. Rabbits were anesthetized and the integrity of the corneal epithelium was inspected using slit lamp microscopy. For the negative (epithelium-on) and positive (epithelium-off) controls, the cornea was presoaked with RF (Epi-on) solution (0.1% RF in PBS) and RF (Epi-off) solution (0.1% RF in 20% Dextran T500 solution) for 30 min. For the experimental groups (epithelium-on), the cornea was presoaked with RF@ZIF-8 composites solutions prepared under different conditions for 30 min. Then, the corneal section light band was evaluated using the cobalt blue light from the slit lamp. The magnification of the slit lamp was set at 16×. Finally, the rabbits were sacrificed by air embolization, and the central 5 mm corneal tissues were immersed in optical cutting temperature compound (OCT) kept at −20 °C and cut into 10 μm-thick sections. The fluorescence images of the resulting sections were captured using a confocal microscope.

In order to choose a proper RF concentration for use in the formation of RF@ZIF-8 composites for subsequent TE-CXL application, five RF concentrations of 2, 4, 6, 8, 10 mg mL⁻¹ in the reaction solutions were selected. After presoaking the cornea for 30 min, the photos and fluorescence images of the central 5 mm corneal tissue were captured. As shown in Figures S11a and S12, Supporting Information, yellow corneal bands could be observed in the photos, and the color of the corneal bands became darker with the increase of RF concentration. When the RF concentration was controlled at 6 mg mL⁻¹, the band became brightest, further increasing the RF concentration resulted in slight reduction of yellow signal. (Figure S11a, Supporting Information); a similar tendency could also be observed in the confocal fluorescence images and fluorescence analysis spectra (Figure S12, Supporting Information). Green luminescent signals could be observed in five

ADVANCED
SCIENCE NEWS
www.advancedsciencenews.com

ADVANCED
MATERIALS
www.advmat.de

samples, indicating that RF could permeate the corneal epithelium using ZIF-8 as a carrier. Meanwhile, the green luminescent signal from the corneal tissue intensified with the enhancement of the RF concentrations with a maximum at 6 mg mL^{-1}, indicating that more RF reached the stroma as RF concentrations increased. However, the trend changed, and the green luminescent signal intensity decreased when the RF concentrations was further increased to 8/10 mg mL^{-1} (Figure S12a, Supporting Information). Fluorescence analysis spectra displayed in Figure S12b, Supporting Information showed the same tendency, the fluorescence intensity of the 6RF@ZIF-8 NF group was highest among the five groups, indicating that the 6RF@ZIF-8 NF system had the best RF corneal epithelial permeability. Variations in the morphology of the composition with different RF concentrations (Figure S7, Supporting Information) are likely responsible for many (but not all) of the observed differences in the absorption effects. It is also possible that, independent of the nanoflakes, which facilitate the release of the RF, the increases in RF concentration alone may be responsible to some extent for the sample substrate becoming more uniform.

Based on the above information, the 6RF@ZIF-8 NF solution (0.26% RF, total) was selected for subsequent studies. Before performing detailed comparisons of 6RF@ZIF-8 NF with RF (Epi-on) (0.1% RF in PBS) and RF (Epi-off) (0.1% RF in 20% Dextran T500 solution), the effect of using RF (Epi-on) with a higher concentration of RF (0.26% RF in PBS, a similar RF concentration as in the 6RF@ZIF-8 NF group) was investigated and the results indicated that increasing the concentration of RF alone could not enhance the RF corneal epithelial permeability (Figure S13, Supporting Information). In addition, 6RF@ZIF-8 NP (6 mg mL^{-1} RF concentration) was selected for comparison in order to study the influence of the morphology of 6RF@ZIF-8 composites on the absorption. Images of the central cornea via slit-lamp photos, confocal fluorescence images, and luminescent spectra assay, and the corneal RF concentration in cornea tissue were measured and the results are shown in Figure S11b, Supporting Information and **Figure 5**. The slit-lamp photos of the cornea presoaked using different samples were studied initially. No green luminescent signal could be observed in the RF (Epi-on) group under cobalt blue light irradiation, indicating that no RF permeated through the corneal epithelium using the RF (Epi-on) solution (0.1% RF in PBS). For the other three groups, including RF (Epi-off), the green luminescent signal could be observed, though the signal intensity varied. The signal intensity of 6RF@ZIF-8 NF (Epi-on) was highest among the three luminescent groups, while the signal intensity of the 6RF@ZIF-8 NP group was the lowest. A similar phenomenon can also be observed in the photos of central cornea displayed in Figure S11b, Supporting Information; the yellow color of the 6RF@ZIF-8 NF group was much darker than the other groups. All of these indicated successful delivery of RF through corneal epithelium and into the stroma using the 6RF@ZIF-8 NF system, which was more effective than 6RF@ZIF-8 NP.

The confocal fluorescence images and fluorescence analysis spectra of the central corneal tissue further confirmed the above observation (Figure 5). No green signal could be found in the confocal fluorescence image in the RF (Epi-on) group, while the green fluorescence signals of the 6RF@ZIF-8 NF

group was highest among the four groups, much higher than that of RF (Epi-off) and 6RF@ZIF-8 NP groups (Epi-on). The fluorescence intensity of the cornea soaked in 6RF@ZIF-8 NF was also highest among the four groups in the fluorescence analysis spectra (Figure 5b). The fluorescence intensity of the four groups was: 6RF@ZIF-8 NF group (Epi-on) > RF (Epi-off) group > 6RF@ZIF-8 NP group (Epi-on) > RF (Epi-on) group, indicating more RF passed through corneal epithelium using 6RF@ZIF-8 NF as the delivery system.

Meanwhile, the RF concentrations in the cornea presoaked with different RF solutions were further measured using a Microplate reader. In this process, the central cornea, without epithelium, was prepared into a corneal homogenate, and further centrifuged to collect the supernatant, which was tested using a Microplate reader. The results are shown in Figure 5c, and further confirmed the above observation. The RF concentration in the cornea for the four groups was: 6RF@ZIF-8 NF group (Epi-on) > RF (Epi-off) group > 6RF@ZIF-8 NP group (Epi-on) > RF (Epi-on) group. All of these indicated that the synthesized 6RF@ZIF-8 NF had better corneal epithelium permeability, and the concentration of RF in the corneal stromal layer was highest among the four groups.

In order to measure the stability of the 6RF@ZIF-8 NP composites, the RF loading efficiency as well as the release rate kinetics of the RF in ZIF-8 with two morphologies (NP and NF) were compared and the results are shown in Figure S14, Supporting Information. Compared with the 6RF@ZIF-8 NP system, it was found that more RF can be encapsulated in 6RF@ZIF-8 NF, the encapsulation efficiency and loading efficiency of RF in 6RF@ZIF-8 NF were higher than in 6RF@ZIF-8 NP (Figure S14a, Supporting Information). Meanwhile, the release rate kinetics of RF were further studied, it can be found that for the same time intervals, the release percentage of RF (%) in 6RF@ZIF-8 NF was little less than that in 6RF@ZIF-8 NP (Figure S14b, Supporting Information). However, for the same amounts of RF (120 mg) added in the raw materials, comparing with 6RF@ZIF-8 NP, more than 54 mg RF can be released from the 6RF@ZIF-8 NF in the first 1 h, especially in the first 0.5 h (Figure S14c, Supporting Information). This is very important for their application in corneal cross-linking as the time of cornea presoaked in RF@ZIF-8 solutions is only 0.5 h. Thus, the higher encapsulation efficiency and more released amount of RF in 6RF@ZIF-8 NF composites in short time interval may have a certain effect to enhance corneal epithelium permeability.

The distribution of Zn^{2+} in the corneal epithelium and stroma was further measured by ICP analysis (average value of 10 cornea) after presoaking the cornea using 6RF@ZIF-8 NF for 30 min. As shown in Figure 5d, compared with that of control groups, the Zn^{2+} content in both the corneal epithelium and stroma was much higher for 6RF@ZIF-8 NF group (Epi-on), indicating the successful permeation of ZIF-8 NF through the corneal epithelium and into the stroma. The degree of increase of Zn^{2+} content in the epithelium was much higher than that in the stroma, indicating more ZIF-8 NF remained in epithelium, which may be attributable to the similar hydrophobic properties of ZIF-8 and the epithelium, resulting in the quick decomposition of ZIF-8 NF and release of RF.
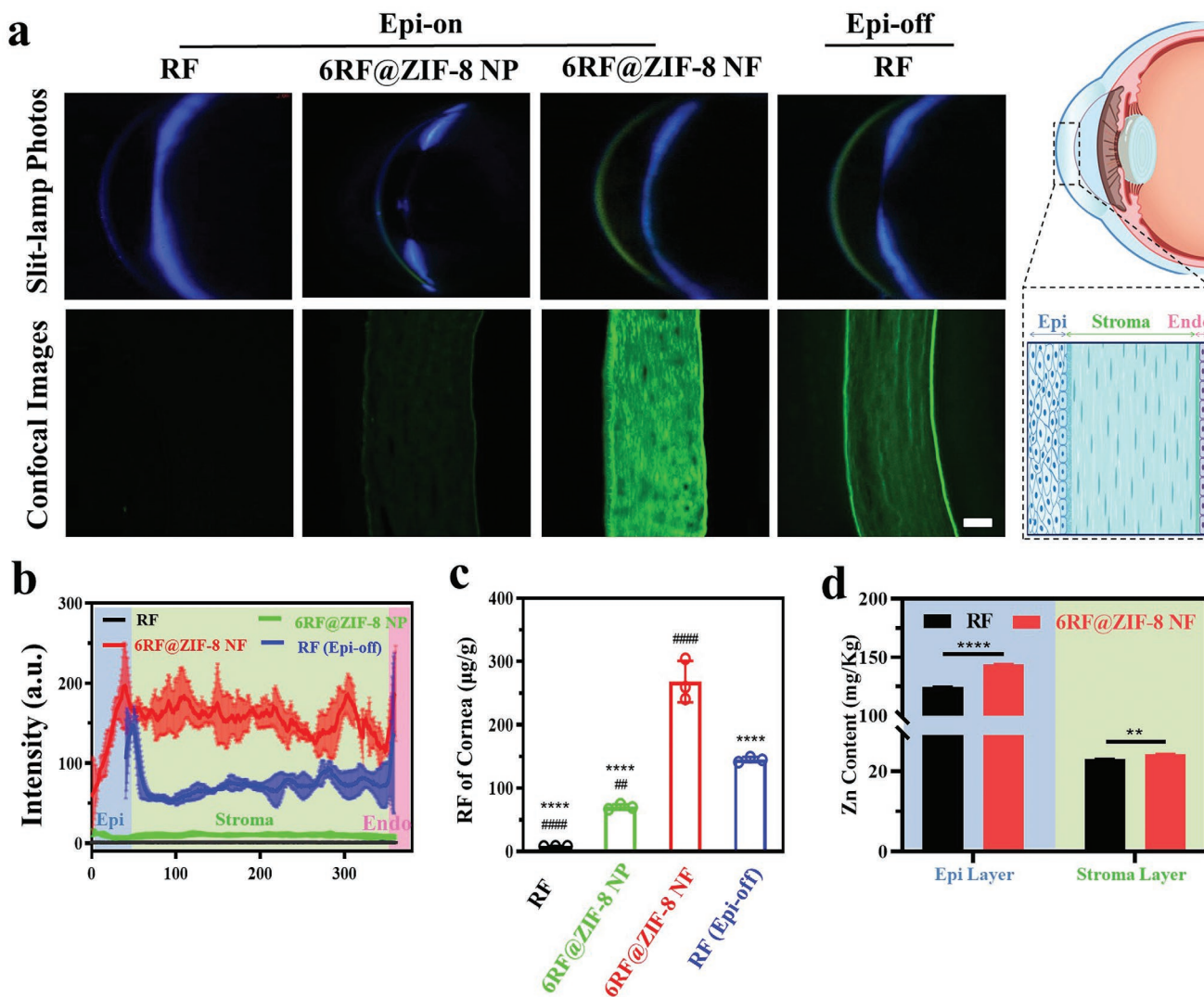
**ADVANCED
SCIENCE NEWS**

www.advancedsciencenews.com

**ADVANCED
MATERIALS**

www.advmat.de

Figure 5. The enhanced permeating capacity of 6RF@ZIF-8 NF into cornea in vivo. a) The RF distribution profile of the cornea using slit-lamp (16×) and confocal microscopy (Scale bar: 100 μm). b) The RF fluorescent qualitative analysis of the cornea from epithelial layer (Epi) to endothelial layer (Endo) in the confocal images (mean ± SD, $n = 3$). c) The quantitation of RF content in the central 8 mm corneal homogenate (mean ± SD, $n = 3$). *indicates the significance of differences between the 6RF@ZIF-8 NF group and each of the other groups; #refers to the significance of differences between the RF (Epi-off) group and each of the other groups (one-way ANOVA with Turkey's multiple comparisons test, $****p < 0.0001$, $##p < 0.01$, $#### p < 0.0001$). d) The tissue distribution of Zn^{2+} in the corneal epithelium and stroma measured by ICP analysis after presoaking the cornea for 30 min (mean ± SD, $n = 3$, unpaired t-test, $**p < 0.01$, $****p < 0.0001$).

Before doing more detailed animal studies, the stability of the 6RF@ZIF-8 NF using different storage methods was also investigated. Lyophilized 6RF@ZIF-8 NF powder, 6RF@ZIF-8 NF aqueous solution, and 6RF@ZIF-8 NF centrifugal precipitation without lyophilization were prepared. The RF distribution profile of the cornea using slit-lamp (16×), confocal microscopy and luminescent spectra of the samples stored for different time intervals were compared, and the results are shown in Figure S15, Supporting Information. The green signal intensity of the confocal microscopy of the lyophilized 6RF@ZIF-8 NF powder groups with 7/15 d storage (Figure S15c, Supporting Information) was similar to the fresh prepared solution group (Figure S15a, Supporting Information), and even higher than that of the RF (Epi-off) group (Figure S15b, Supporting

Information), demonstrating the excellent corneal epithelial permeability of 6RF@ZIF-8 NF even after lyophilized treatment. In contrast, 6RF@ZIF-8 NF aqueous solution and 6RF@ZIF-8 NF centrifugal precipitation without lyophilization could only be stored for about 7 d after which the transepithelial ability decreased, and when the storage time was prolonged to 9 d, only a very weak green luminescent signal could be observed (Figure S15d,e, Supporting Information). A similar tendency could also be found in the slit-lamp images. The fluorescence analysis spectra of the cornea soaked in 6RF@ZIF-8 NF with different treatment for 7 d were further compared directly (Figure S15f, Supporting Information), which confirmed the differences among the three storage methods. The fluorescence intensity of the groups was: Fresh solution

**ADVANCED
SCIENCE NEWS**

www.advancedsciencenews.com

**ADVANCED
MATERIALS**

www.advmat.de

> lyophilized powder > RF (Epi-off) > Aqueous solution > Centrifugal precipitation. When compared with the 6RF@ZIF-8 NF aqueous solution and the 6RF@ZIF-8 NF centrifugal precipitation without lyophilization, the lyophilized 6RF@ZIF-8 NF powder was found to have better stability and could be stored for a longer time, with slightly better transepithelial ability than RF (Epi-off) (0.1% RF in 20% Dextran T500 solution). These results indicated the 6RF@ZIF-8 NF can stored for a reasonable time and this facilitates its further clinical application.

Combining the above data with the SEM images in Figure 1 and Figure S7, Supporting Information, it was concluded that the morphology of the 6RF@ZIF-8 composites could influence the corneal epithelial permeability of RF. The experimental results indicated that 6RF@ZIF-8 NF had a better corneal RF absorption effect than 6RF@ZIF-8 NP. We believe this to be due to the special hibiscus-like structure, which consisted of 2D flake petals adhered to each other. The special structure of 6RF@ZIF-8 NF allows it to have a larger contact area with the epithelium than the individual nanoparticles. The imperfect crystal structure of 2D flakes facilitates the decomposition of 6RF@ZIF-8 NF into smaller pieces, while the similarity of the hydrophobicity of 6RF@ZIF-8 NF to that of the corneal epithelium facilitates its decomposition and the quick dissociation of RF from ZIF-8 NF in the corneal epithelium (the higher distribution of Zn^{2+} in the corneal epithelium confirmed this speculation). On the other hand, though 6RF@ZIF-8 NP is smaller than 6RF@ZIF-8 NF, its perfect crystal structure required more time for it to decompose and for the RF within the nanoparticles to release to the surface. Furthermore, the relatively lower contact area of 6RF@ZIF-8 NP with the epithelium allows these particles to be easily washed away from the ocular surface by the tear film. Based on the above information, we believe that more metal–organic framework nanomaterials with excellent properties may be found and used as the carrier of RF in the future. We think that if the MOF nanomaterials meet with the following conditions, such as: synthesis at room temperature (RF is not stable at high temperature), tunable morphology, positive potential, hydrophobicity, good biocompatibility and biodegradability, they could be used as candidate carriers for RF.

2.4. Biocompatibility of RF@ZIF-8 Composites

Based on the above information, the 6RF@ZIF-8 NF solution was chosen for subsequent investigation. Alizarin Red S and Trypan Blue staining of the endothelium, Hematoxylin-Eosin staining of the cornea as well as TUNEL staining were performed, and the results are shown in Figure 5. As shown by the endothelium staining (ES) in **Figure 6**, like RF (Epi-on) and RF (Epi-off) groups, no blue cells could be observed in the 6RF@ZIF-8 NF group, indicating that all cells remain alive. The intact endothelial structure further indicates the healthy state of the cells in the 6RF@ZIF-8 NF group, further confirmed by the statistical analysis of ES photos (Figure S16, Supporting Information). Meanwhile, the yellow color of the endothelial cell was darker for 6RF@ZIF-8 NF than the other two groups, indicating that more RF had successfully reached the stroma. The Hematoxylin-Eosin staining results are also shown in Figure 6.

As with the RF (Epi-on) group, no damage can be observed in the 6RF@ZIF-8 NF group, indicating that the obtained composites can deliver RF to permeate the corneal epithelium without damaging epithelial cells. This phenomenon is of great significance for clinical applications, as many researchers have indicated that riboflavin reagents used for TE-CXL function mainly by destroying the epithelium, while for the RF (Epi-off) group, no epithelial cells are present as they are removed before soaking. Furthermore, the corneal stromal layers in the three groups were also compared; all cells in this layer were arranged well and no obvious cell damage was observed, indicating excellent biocompatibility of 6RF@ZIF-8 NF. Due to the removal of the corneal epithelium, the corneal thickness of the RF (Epi-off) group was lowest, while little difference could be observed for the RF (Epi-on) and 6RF@ZIF-8 NF groups due to the preservation of the corneal epithelium, which further decreases the risks of tissue photo-damage during CXL.

TUNEL staining of cornea was carried out to assay the apoptosis of the synthesized 6RF@ZIF-8 NF and the results are shown Figure 6 with the standard positive and negative group displayed in Figure S17. No green color can be observed in the image of the 6RF@ZIF-8 NF group, indicating that like the RF (Epi-on) and RF (Epi-off) groups, the synthesized 6RF@ZIF-8 NF did not induce apoptosis, which further confirmed the excellent biocompatibility of the synthesized 6RF@ZIF-8 NF. All of the above characterizations indicated that there was no harm to the epithelium, stroma and endothelial layer for the 6RF@ZIF-8 NF.

2.5. Evaluation of CXL

The results of the in vivo CXL evaluation are shown in **Figure 7**. The operation procedure is shown in Figure 7a. After being presoaked for 30 min using various RF solutions, 365 nm of continuous UVA (3 mW cm^{-2} power density) applied to an 8 mm facula was used to irradiate the cornea for 30 min, adding one drop of the corresponding RF solutions every 5 min (Figure S18, Supporting Information). After that, enzymatic digestion of collagen and stress-strain measurements were performed to evaluate the CXL effect.

Figure 7b displays the photos of the corneal tissue residues after enzymatic digestion of corneal collagen. The cornea was soaked in 3 mL 0.2% Collagenase Type 2 solution under constant shaking, and the photos of corneal tissue residues obtained at different soaking time after CXL were taken. A time of 7 h was required for the cornea tissues to dissolve completely for the RF (Epi-on) group, while the digestion trends of corneal tissue for the 6RF@ZIF-8 NF group (Epi-on) and the RF (Epi-off) group were similar and both took about 40 h, with further prolonging of the soaking time resulting in little change in the area of the residues. The statistical analysis showed in Figure 7c also indicated similar results. After soaking for 48 h, the disc area of residual cornea was ≈16% of initial state in 6RF@ZIF-8 NF and positive group. The dry weight of the residual cornea reached balance (no change in the disc area with prolonged soaking time) and the time for the disc area to reach balance (the time after which there was no variation in the residual cornea disc area) were measured and are
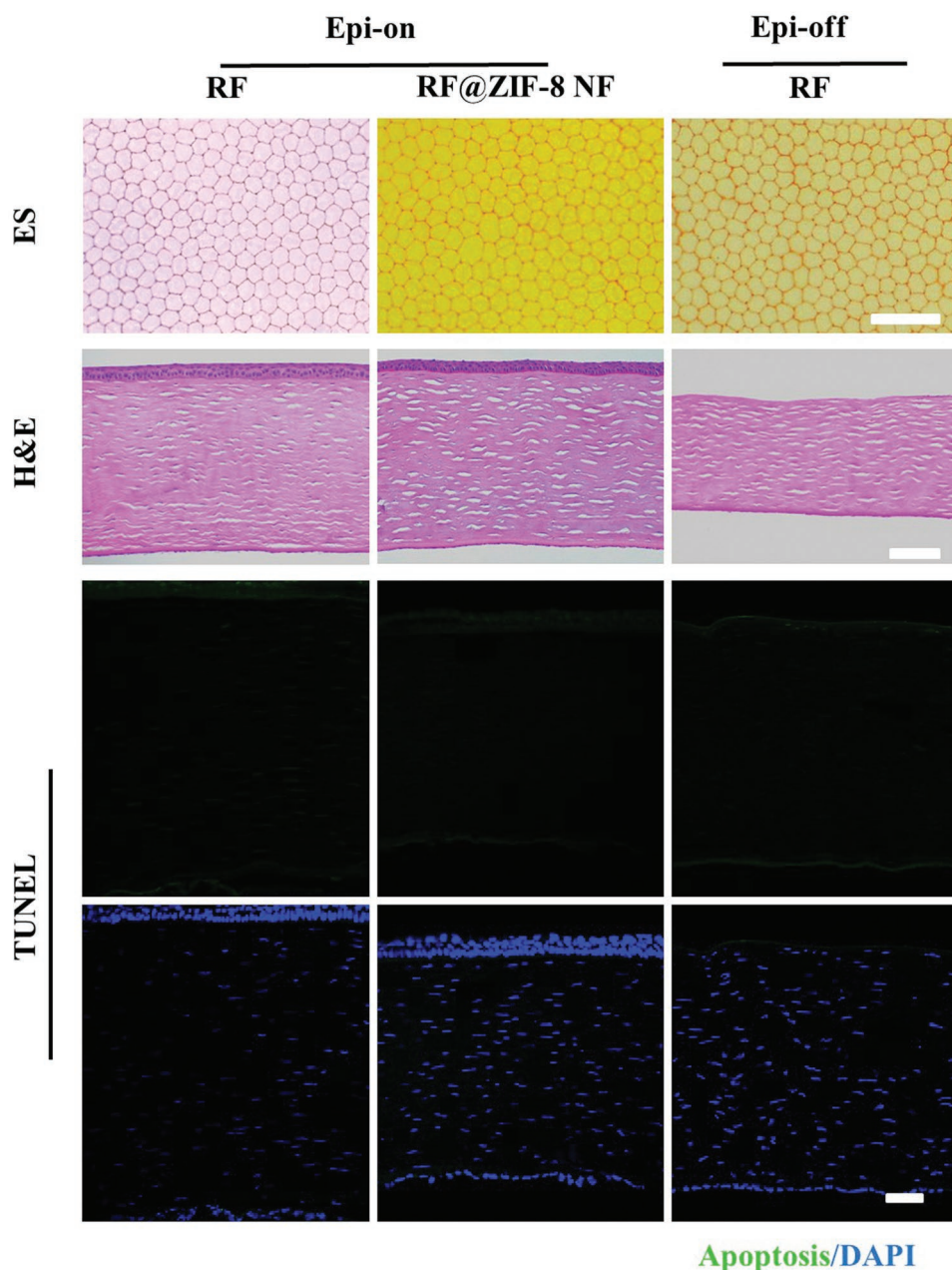
Figure 6. The histopathologic observation of the toxicity of RF@ZIF-8 NF on the cornea in vivo. Endothelial staining (ES), Hematoxylin-Eosin staining (H&E) and TUNEL test of cornea after being soaked with RF (Epi-on), 6RF@ZIF-8 NF (Epi-on), and RF (Epi-off) for 30 min. Scale bar: 100 μm.

shown in Figure S19, Supporting Information. The dry weight and balance time of disc area of 6RF@ZIF-8 NF group was similar with that of RF (Epi-off) group, indicating the outstanding TE-CXL effect of the 6RF@ZIF-8 NF group.

Stress-strain measurements were performed to evaluate the TE-CXL effect in the 6RF@ZIF-8 NF group. After CXL, the corneas were cut into 10 mm × 3 mm strips along the 12:00 to 6:00 direction. Each strip was fixed vertically into the stretching equipment. The pre-cycling tensile strength was set as 0.5 N, and the tensile displacement was 1 mm at a rate of 2 mm/min, then returned to 0 at the same rate with a suspension of 30 s for three cycles. Later, each cornea was stretched to 20%

deformation immediately at a loading rate of 2 mm min^{-1}. The stress–strain curves are shown in Figure 7d,e. The stress and Young's modulus of the 6RF@ZIF-8 NF group was higher than other two groups at the same strain, indicating better biomechanical properties of the cornea after TE-CXL with 6RF@ZIF-8 NF as the delivery system.

Based on the above information, it was concluded that the TE-CXL effect of the 6RF@ZIF-8 NF was better than the C-CXL of RF (Epi-off) group. Thus, the use of this reagent can relieve the post-operative ocular pain and decrease the risk of infectious keratitis. Meanwhile, the higher luminescence intensity of the 6RF@ZIF-8 NF group in the confocal fluorescence images
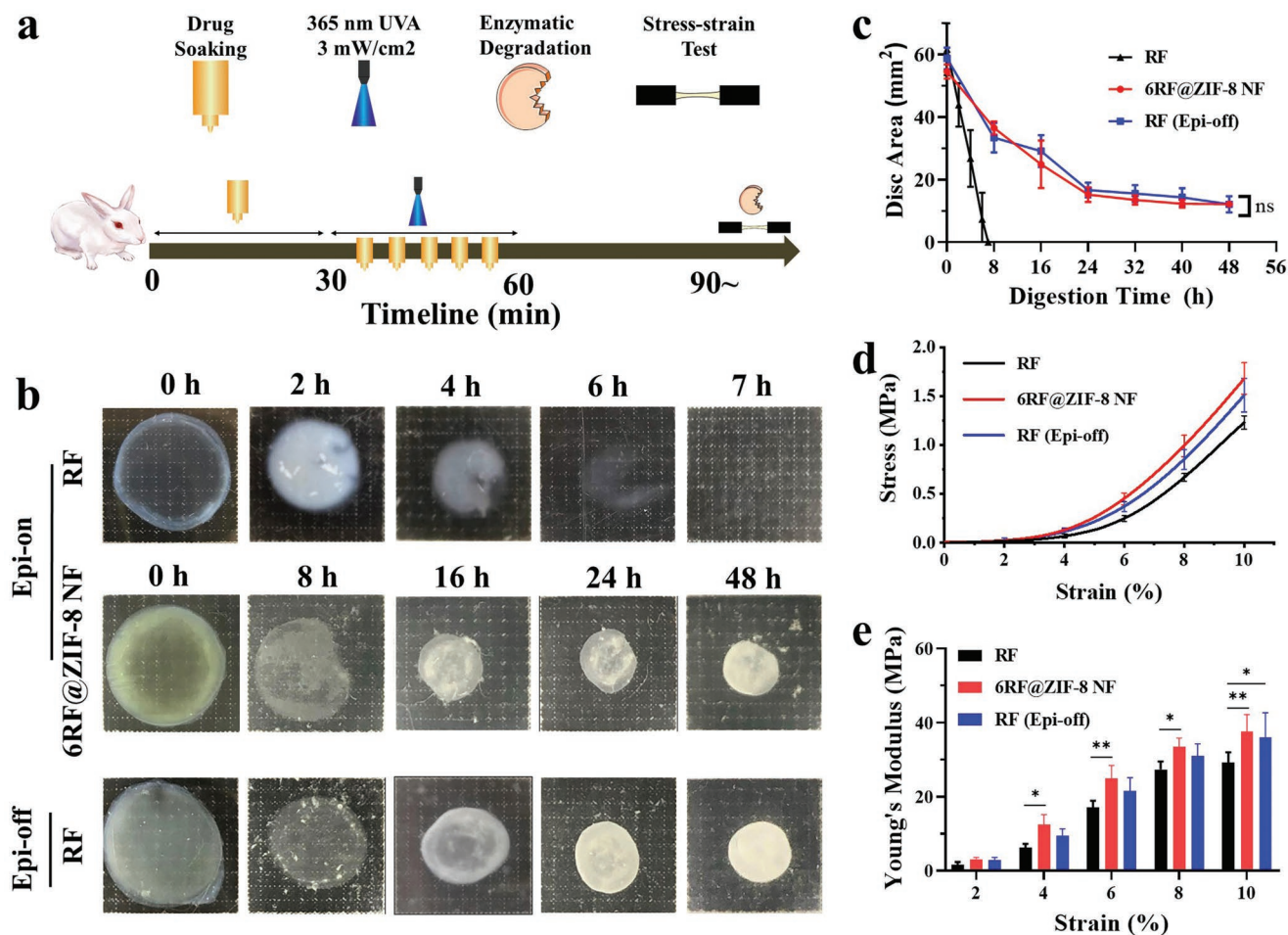
2109865 (13 of 17)

Figure 7. The in vivo CXL evaluation. a) The operation procedure of in vivo CXL evaluation. b) The photos of cornea digestion behavior in the collagenase II. c) Statistic analysis of the disc area as a function of time (mean ± SD, $n = 4$, the disc area of 6RF@ZIF-8 NF group and RF (Epi-off) group at the same timepoint were compared using two-way ANOVA with Sidak's multiple comparisons test, ns: no significance). d,e) The biomechanical property of cornea (mean ± SD, $n = 4$, two-way ANOVA with Turkey's multiple comparisons test, $*p < 0.05$, $**p < 0.01$).

indicated a higher RF concentration in the corneal tissue, which could also decrease the risk of photo-damage during UVA irradiation.

3. Conclusion

In summary, a novel TE-CXL agent, hibiscus-like 6RF@ZIF-8 NF microsphere composites, was successfully synthesized using a one-pot synthesis method. It has the property of being hydrophobic, with a high surface area loading capacity. ZIF-8 as a carrier was capable of delivering hydrophilic RF to permeate the hydrophobic corneal epithelium with its negative potential surface proteins and reach the corneal stroma. The TE-CXL effect of this reagent was better than that of the C-CXL protocol with a central 7–9 mm of corneal epithelium removed, indicating the potential application in clinical settings. The special hibiscus-like structure of 6RF@ZIF-8 NF has a greater TE-CXL effect than that of 6RF@ZIF-8 NP nanoparticles. Thus, the 6RF@ZIF-8 NF composites have a potential application in TE-CXL for corneal ectasias.

4. Experimental Section

Materials and Reagents: Zinc nitrate hexahydrate ($Zn(NO3)2.6H2O$), 2-methylimidazole (2-mim), methanol, potassium bromide (KBr), magnesium acetate tetrahydrate, and trichloroacetic acid were purchased from Aladdin Industrial Inc. Riboflavin 5'-phosphate sodium (RF), Trypan Blue, and Alizarin Red S were purchased from Sigma–Aldrich (MI, Italy). The reagents for Positive Control Preparation Kit for TUNEL Assay and In Situ Cell Death Detection Kit Fluorescein were purchased from Beyotime. Dextran T500 was purchased from Shanghai Yuanye Bio-Technology Co. Collagenase Type 2 was purchased from Worthington Biochemical Corporation. All reagents used in this study were used as received without further purification.

Synthesis of ZIF-8 As Well As RF@ZIF-8 Composites: *Synthesis of ZIF-8 Nanoparticles (ZIF-8 NP)*: For a typical synthesis process of ZIF-8 NP, 240 mg $Zn(NO_3)_2.6H_2O$ was first dissolved in 10 mL methanol while stirring, until a transparent solution was obtained, then, 10 mL methanol containing 480 mg 2-mim was added into the above solution. After being stirred for 4 h at room temperature, the reaction mixture was maintained for 12 h. Finally, the product was collected by centrifugation and washed three times with ethanol.

Synthesis of ZIF-8 NF: The synthesis procedures were similar with that of ZIF-8 NP except the masses of raw materials ($Zn(NO_3)_2$ and 2-mim) were decreased with different ratio. For example, the sample of ZIF-8 NF

can be obtained using 60 mg of $Zn(NO_3)_2.6H_2O$ and 120 mg of 2-mim as raw materials with other reaction conditions unchanged.

Synthesis of Hibiscus-Like RF@ZIF-8 Microspheres Composites (6RF@ZIF-8 NF): The synthesis procedures of RF@ZIF-8 composites were similar with that of ZIF-8 NF except different amounts of RF were dissolved in 2-mim methanol solution. For example, 6RF@ZIF-8 NF can be obtained by adding 120 mg RF into 10 mL 2-mim methanol solution with others reaction conditions the same to those of ZIF-8 NF. 2RF@ZIF-8, 4RF@ZIF-8, 8RF@ZIF-8, 10RF@ZIF-8 composites are obtained by adding 40, 80, 160, and 200 mg RF into a 10 mL 2-mim methanol solution with other reaction conditions unchanged.

Synthesis of 6RF@ZIF-8 Nanoparticles (6RF@ZIF-8 NP): The synthesis procedures of 6RF@ZIF-8 NP composites were similar with that of 6RF@ZIF-8 NF except that 240 mg $Zn(NO_3)_2.6H_2O$ and 480 mg 2-mim were added into the reaction system.

The Encapsulation and Loading Efficiency of RF in 6RF@ZIF-8 NF and 6RF@ZIF-8 NP: The reaction mixture maintained for 12 h was first centrifuged at 12 000 rpm for 10 min, and methanol supernatant was collected and labeled ①. Then, the precipitation was washed with 20 mL ethanol for three times, and the supernatant were further collected by centrifugation at 12 000 rpm for 10 min each time and labeled as ②, ③, ④, respectively. The standard curve of RF in methanol and ethanol solvent was measured with a microplate reader, and then the absorbance of RF in supernatant (①–④) was measured to calculate their RF content. The amount of RF loaded in ZIF-8 NF and ZIF-8 NP can be calculated by subtracting the amount of RF in supernatant from the total amount of RF added in the reaction. Meanwhile, the obtained precipitation was lyophilized to calculate the loading efficiency.

The encapsulation efficiency(EE%) and loading efficiency(LE%) of RF was calculated following the equation:

$$EE\% = \left(W_{total} - W_{sup}\right)/W_{total} \times 100\% \tag{1}$$

$$LE\% = \left(W_{total} - W_{sup}\right)/W_{pre} \times 100\% \tag{2}$$

where W_{total} is the total amount of RF added in the reaction, W_{sup} is the amount of RF in supernatant, while the W_{pre} is the amount of the lyophilized precipitation.

The RF Release of 6RF@ZIF-8 NF and 6RF@ZIF-8 NP: The measurements of RF release of 6RF@ZIF-8 NF and 6RF@ZIF-8 NP were performed by dispersing 6RF@ZIF-8 NF and 6RF@ZIF-8 NP in to 10 mL deionized water under gentle shaking in shaker. The samples were centrifuged (12 000 rpm min^{-1}, 10 min) to collect the supernatant at the certain time intervals, and the absorbance of RF in the supernatant were measured using a microplate reader monitored at 460 nm. The amount of RF were further calculated by comparing with the standard curve of RF aqueous solution. Then, 10 mL deionized water was added to the precipitation for further measurement. The time intervals were controlled at 0, 0.5, 1, 2, 4, 6, and 8 h.

Animal Evaluations: Male Japanese white-eared rabbits (weight, 2.0–2.5 kg) were raised with free accessed to food and water throughout the test period. The animal study was approved by the Ethical Committee of EYE and ENE Hospital of Fudan University (IACUC-DWZX-2021-012).

The Corneal Riboflavin Absorption: First, the integrity of the corneal epithelium was inspected using slit lamp biomicroscopy (Kanghua, China). Then, xylazine hydrochloride (0.2 mL kg^{-1}) and 2% pentobarbital sodium (1 mL kg$^-$) were injected to anesthetize the rabbits via intramuscular injection. For the RF (Epi-on) and RF (Epi-off) (the corneal epithelium was removed by a blunt knife) controls, 0.1% RF in PBS solution and the 0.1% RF in 20% Dextran T500 solution was used to presoak the cornea for 30 min, respectively; For the experimental groups (Epi-on), fractional centrifugation was used to separate big particles from the samples (5000 rpm min^{-1}, 10 min), and the upper solution with total volume controlled at 20 mL (diluted using deionized water to control the total volume) was collected. The concentration of the 6RF@ZIF-8 NF was measured to be 3.1 mg mL^{-1} through dry weight, while the concentration of RF in the 6RF@ZIF-8 NF solution was measured to be about 2.6 mg mL^{-1} through microplate reader by 20× dilution and compared with standard curve of RF aqueous solution. The cornea was presoaked in solutions containing RF@ZIF-8 at different conditions for 30 min. Then, the corneal section light band was evaluated using a slit lamp with cobalt blue light immediately after absorption. The rabbits were sacrificed by air embolization, and the central 5 mm corneal tissue was frozen in OCT and cut into 10 µm-thick sections. The fluorescence images of the sections were captured with a confocal microscope (Zeiss LSM710).

RF Concentration Analysis: *Slit Lamp Photography*: Immediately after absorption with different RF solutions, a slit lamp with cobalt blue light was used to record the intensity of corneal RF fluorescence, the magnification of slit lamp was set at 16×. Then, the rabbits were sacrificed for the following tests.

Single Photon Confocal Microscopy: In each group, the central 5 mm cornea of the treated eyes were immersed in optical cutting temperature compound (OCT) kept at −20 °C and cut into 10 µm-thick sections vertically. The RF fluorescence was excited at 488 nm and emission detected in the range 491–556 nm with single photon confocal microscopy (Olympus FluoView 1000 confocal microscope; Olympus America Inc., Center Valley, PA). The RF intensity profile was determined by averaging the signal using Image J software.

Quantitative Analyses of RF Concentration Using a Microplate Reader: In each group, the central 8 mm corneal stroma was trephined. The corneal homogenate was prepared by ball milling followed by incubation in 15 mmol L^{-1} magnesium acetate tetrahydrate at 65 °C for 15 min. Then, 10% trichloroacetic acid was added to remove the protein. The volume ratio of the corneal homogenate: magnesium acetate tetrahydrate: trichloroacetic acid was 2:2:1. The mixture was then centrifuged (12 000 rpm, 5 min, 4 °C) and the supernatant was collected, which was further tested by means of the microplate reader (Spectramax M5, Molecular Devices, US) monitored using 435 nm excitation wavelength and 525 nm emission wavelength.

Stability Measurement of 6RF@ZIF-8 NF with Different Storage Methods: Lyophilized 6RF@ZIF-8 NF powder, 6RF@ZIF-8 NF aqueous solution, and 6RF@ZIF-8 NF centrifugal precipitation without lyophilization were prepared and stored at 4 °C in a refrigerator. Before animal corneal riboflavin absorption evaluation, lyophilized 6RF@ZIF-8 NF powder and centrifugal precipitation were dispersed into deionized water with the same concentration as the 6RF@ZIF-8 NF aqueous solution (0.26 mg mL^{-1} RF), with other procedures the same as above, and the slit-lamp and confocal microscopy of 6RF@ZIF-8 NF with different storage methods and different time intervals (1, 2, 3, 5, 7, 9, 15 d) were carried out.

Quantitative Analyses of Zn^{2+} Concentration Using ICP: In this part, both eyes of each rabbit were divided into two groups (experimental and control), resulting in ten specimens per group. For the experimental group, after the cornea had been presoaked using 6RF@ZIF-8 NF for 30 min, the cornea was trephined and divided into epithelium and stroma. Then, the homogenate of each part was prepared by ball milling and lyophilized into power before measurement. For the control group, a similar operation was executed for the other eye of each rabbit with the exception of presoaking.

In Vivo Biocompatibility: *Alizarin Red S and Trypan Blue Staining of Endothelium*: As with the absorption experiment mentioned above, the solutions with different contents were presoaked over the cornea for 30 min. Subsequently, the central 5 mm cornea was trephined and placed on a glass slide with the endothelium side up. Then, 0.2% trypan blue was dropped to cover the endothelium for 90 s; the cornea was then washed 2–3× using PBS, and drained gently to remove excess solution. After that, the endothelial layer was dropped with alizarin red S (0.2%, pH 4.7) for another 90 s and rinsed two or three times using PBS. Finally, the microscope (Leica DM750) was used to observe the morphology of the endothelium.

Hematoxylin-Eosin Staining of Cornea: In this part, the rabbits were killed by air embolization after riboflavin absorption and the corneas were removed immediately and transferred into fixation liquid for 2 h. The fixation liquid was composed of 80% ethanol, 10% acetic acid and 10% formaldehyde. After undergoing a series of dehydration steps, hematoxylin was first added dropwise to cover the section for 10 min

which was then washed with PBS. Finally, eosin was used for staining the extracellular matrix for 8 min. and the corneal epithelium and stromal cells were observed in the light microscope (Leica DM750).

TUNEL Staining of Cornea: Apoptosis assay was done by TUNEL staining. The assay was carried out on central 10 µm-thick corneal sections using an apoptosis detection kit (In situ cell death detection kit, Fluorescein) following the manufacturer's instructions. The TUNEL-positive control was also performed according to the instructions using Positive control preparation kit.

In Vivo CXL Evaluation: After being presoaked for 30 min, 365 nm of continuous UVA (3 mW cm^{-2} power density) and an 8 mm diameter facula was used to irradiate the cornea for 30 min, adding one drop of the same solution every 5 min in case of volatilization. After that, enzymatic digestion and stress-strain measurement were performed to evaluate the CXL effect; the details were as follows:

Enzymatic Digestion of Collagen: After CXL, the central 8 mm of the cornea was trephined and soaked in 3 mL 0.2% Collagenase Type 2 solution under constant shaking (175 rpm, 37 °C) until the remaining tissue had undergone complete digestion. During the digestion process, the remaining corneal tissues of the experimental group and RF (Epi-off) group were monitored every 8 h by capturing pictures. The pictures of RF (Epi-on) groups were captured every 1 h. The corneal area was measured using Image J and the curve of the residual corneal area was drawn. Meanwhile, the dry weight and area balance time of the cornea tissues after collagenase II digestion were calculated.

Stress–Strain Measurement: After 30 min of UVA corneal crosslinking, a tailor-made double-bladed cutter was used to cut the cornea into 10 mm × 3 mm strips. Each strip was fixed vertically in the pneumatic jaws of stretching equipment (Instron 68TM-30, Instron INC., MA, USA), and all measurements were initiated with tissue preconditioning. The pre-cycling tensile load was 0.5 N, and the tensile displacement was 1 mm at 2 mm min^{-1}, then returned to 0 at 2 mm min^{-1}, for three cycles with an interval of 30 s. Finally, each cornea was stretched to 20% deformation immediately, at a loading rate of 2 mm min^{-1}, the stress–strain curves were drawn, and the Young's modulus was determined as the linear portion with each slope of the curves, expressed in MPa.

Other Characterizations: The phase structure and crystallographic state of the obtained ZIF-8 nanomaterials and RF@ZIF-8 composites were investigated by a Smartlab 9 powder Diffractometer with Cu K radiation ($\lambda = 1.54$ Å). The morphology and microstructure were inspected using a field emission scanning electron microscope (HITACHI S-7400, Japan) and a high resolution transmission electron microscopy (JEM2100F, Japan) with an accelerating voltage of 200 kV. The surface functional groups of the products were investigated through FT-IR spectra ranging from 400 to 4000 cm^{-1}, operated on a Thermal Fisher Nicolet 6700 spectrometer (USA) with KBr pellet technique. Elements analysis were recorded on Elementar Elemental analyzer (UNICUBE, German). BET measurements were performed on a surface area and porosimetry analyzer (QUANTACHROME, USA). The excitation and emission spectra were recorded by a Hitachi F-7000 Fluorescence Spectrophotometer (Japan). Zeta potential was obtained by Malvern ZETASIZER equipment (Nano-ZS90, UK). The TG-DSC curves were recorded by a TA Discovery SDT 650 Synchronous thermal analyzer (USA). High temperature XRD patterns were recorded by Empyrean X-ray powder Diffractometer (Holland). XPS experiments were carried out using a Thermo SCIENTIFIC ESCALAB 250Xi spectrometer. The spectra were recorded using monochromatic Al Kα radiation (hv = 1486.6 eV) as the excitation source. The test spot area was 500 µm with tube current controlled at 10 mA. Photoelectrons were selected in energy with a hemispheric electron analyzer. All of the binding energy (BE) values were referenced to the C 1s peak of carbon at 284.6 eV. ICP-MS analysis was performed on Agilent 720 system.

Statistical Analysis: All data were shown as the mean ± standard deviation (means ± SD). The significance between groups was determined by Graphpad Prism 8.0 software using unpair t-test, one-way analysis of variance (ANOVA) or two-way ANOVA (ns: no significance; $*p < 0.05$, $**p < 0.01$, $***p < 0.001$, $****p < 0.0001$). Specific sample size, comparisons method and other details were indicated in each figure legend.

Supporting Information

Supporting Information is available from the Wiley Online Library or from the author.

Conflict of Interest

The authors declare no conflict of interest.

Data Availability Statement

The data that support the findings of this study are available from the corresponding author upon reasonable request.

[1] J. H. Krachmer, R. S. Feder, M. W. Belin, *Surv. Ophthalmol.* **1984**, *28*, 293.

[2] G. Wollensak, E. Spoerl, T. Seiler, *J. Cataract Refract. Surg.* **2003**, *29*, 1780.

[3] G. R. S. Franzco, *Clin. Exp. Ophthalmol.* **2010**, *38*, 141.

[4] G. Wollensak, E. Spoerl, T. Seiler, *Am. J. Ophthalmol.* **2003**, *135*, 620.

[5] G. Wollensak, *Curr. Opin. Ophthalmol.* **2006**, *17*, 356.

[6] M. K. Smolek, W. H. Beekhuis, *Invest Ophthalmol. Vis. Sci.* **1997**, *38*, 1289.

[7] C. Mazzotta, T. Caporossi, R. Denaro, C. Bovone, C. Sparano, A. Paradiso, S.t. Baiocchi, A. Caporossi, *Acta Ophthalmol.* **2012**, *90*, 259.

[8] C. Koppen, J. C. Vryghem, L. Gobin, M. J. Tassignon, *J. Refract. Surg.* **2009**, *25*, 819.

[9] M. Pollhammer, C. Cursiefen, *J. Cataract Refract. Surg.* **2009**, *35*, 588.

[10] A. Kissner, E. Spoerl, R. Jung, K. Spekl, L. E. Pillunat, F. Raiskup, *Curr. Eye Res.* **2010**, *35*, 715.

[11] D. Z. Wen, Q. Li, B. H. Song, R. X. Tu, Q. M. Wang, D. P. S. O'Brart, M. A. Colm, J. H. Huang, *Invest Ophthalmol. Vis. Sci.* **2018**, *59*, 3920.

[12] D. M. Gore, D. O'Brart, P. French, C. Dunsby, B. D. Allan, *Invest Ophthalmol. Vis. Sci.* **2015**, *56*, 5006.

[13] C. Caruso, C. Ostacolo, R. L. Epstein, G. Barbaro, S. Troisi, D. Capobianco, *Cornea* **2016**, *35*, 145.

[14] G. Lombardo, S. Serrao, M. Lombardo, *Graefes Arch. Clin. Exp. Ophthalmol.* **2020**, *258*, 829.

[15] L. Mastropasqua, M. Nubile, R. Calienno, P. A. Mattei, E. Pedrotti, N. Salgari, R. Mastropasqua, M. Lanzini, *Am. J. Ophthalmol.* **2014**, *157*, 623.

[16] R. Lamy, E. Chan, H. Zhang, V. A. Salgaonkar, S. D. Good, T. C. Porco, C. J. Diederich, J. M. Stewart, *Invest Ophthalmol. Vis. Sci.* **2013**, *54*, 5908.

[17] R. S. Rubinfeld, C. Caruso, C. Ostacolo, *Cornea* **2019**, *38*, 780.

[18] D. Wen, B. Song, Q. Li, R. Tu, Y.i. Huang, Q. Wang, C. McAlinden, D. O'Brart, J. Huang, *Cornea* **2018**, *37*, 1018.

[19] D. A. Godefrooij, S. L. Roohé, N. Soeters, R. P. L. Wisse, *Cornea* **2020**, *39*, 63.

[20] M. Iqbal, A. Elmassry, H. Saad, A. A. Gad, O. Ibrahim, N. Hamed, A. Saeed, A. S. Khalil, M. Tawfik, A. Said, I. Amer, A. Nooreldin, O. Said, M. Reffat, S. Anwar, A. Badawi, *Acta Ophthalmol.* **2020**, *98*, e352.

[21] C. Labate, M. Lombardo, G. Lombardo, M. P. D. Santo, *Invest Ophthalmol. Vis. Sci.* **2017**, *58*, 179.

[22] P. W. J. Morrison, C. J. Connon, V. V. Khutoryanskiy, *Mol Pharm.* **2013**, *10*, 756.

[23] K. M. Bottos, A. G. Oliveira, P. A. Bersanetti, R. F. Nogueira, A. A. S. Lima-Filho, J. A. Cardillo, P. Schor, W. Chamon, *PLoS One* **2013**, *8*, e66408.

[24] G. Lombardo, N. L. Micali, V. Villari, N. Leone, S. Serrao, D. Rusciano, M. Lombardo, *J. Cataract Refract. Surg.* **2017**, *43*, 680.

[25] K. Ohmin, J. Y. Kim, S. Park, J. H. Lee, J. Ha, H. Park, H. R. Moon, J. Kim, *Nat. Commun.* **2019**, *10*, 3620.

[26] J. Yang, Y. W. Yang, *Small* **2020**, *16*, 1906846.

[27] K. Shen, L. Zhang, X. Chen, L. Liu, D. Zhang, Y. Han, J. Chen, J. Long, R. Luque, Y. Li, B. Chen, *Science* **2018**, *359*, 206.

[28] C. He, K. Lu, D. Liu, W. Lin, *J. Am. Chem. Soc.* **2014**, *136*, 5181.

[29] P. Horcajada, R. Gref, T. Baati, P. K. Allan, G. Maurin, P. Couvreur, G. Férey, R. E. Morris, C. Serre, *Chem. Rev.* **2012**, *112*, 1232.

[30] S. Y. Teresa, A. Mielcarek, P. Couvreur, C. Serre, *Adv. Mater.* **2018**, *30*, 1707365.

[31] J. Sun, J. Wan, Y. Wang, Z. Yan, Y. Ma, S. Ding, M. Tang, Y. Xie, *J. Hazard. Mater.* **2022**, *429*, 128299.

[32] M. Al Sharabati, R. Sabouni, G. A. Husseini, *Nanomaterials* **2022**, *12*, 277.

[33] J. D. Rocca, D. Liu, W. Lin, *Acc. Chem. Res.* **2011**, *44*, 957.

[34] C. Y. Sun, C. Qin, X. L. Wang, G. S. Yang, K. Z. Shao, Y. Q. Lan, Z. M. Su, P. Huang, C. G. Wang, E. B. Wang, *Dalton Trans.* **2012**, *41*, 6906.

[35] X. C. Huang, Y. Y. Lin, J. P. Zhang, X. M. Chen, *Angew Chem. Int. Ed. Engl.* **2006**, *45*, 1557.

[36] K. S. Park, Z. Ni, A. P. Cote, J. Y. Choi, R. Huang, F. J. Uribe-Romo, H. K. Chae, M. O' Keeffe, O. M. Yaghi, *Proc. Natl. Acad. Sci. U. S. A.* **2006**, *103*, 10186.

[37] M. R. Broadley, P. J. White, J. P. Hammond, I. Zelko, A. Lux, *New Phytol.* **2007**, *173*, 677.

[38] E. Ren, L. Zhang, J. An, T. Wang, L. Li, X. Si, L. He, X. Wu, C. Wang, Z. Su, *Chem. Commun.* **2014**, *50*, 1000.

[39] Y. Hu, H. Kazemian, S. Rohani, Y. Huang, Y. Song, *Chem. Commun.* **2011**, *47*, 12694.

[40] K. Cheng, F. Svec, Y. Lv, T. Tan, *Small* **2019**, *15*, 1902927.

[41] S. X. Yang, W. P. Zhu, Z. P. Jiang, Z. X. Chen, J. B. Wang, *Appl. Surf. Sci.* **2006**, *252*, 8499.

[42] S. X. Yang, Y. J. Feng, J. F. Wan, W. P. Zhu, Z. P. Jiang, *Appl. Surf. Sci.* **2005**, *246*, 222.

[43] W. T. Yao, S. H. Yu, Y. Zhou, J. Jiang, Q. S. Wu, L. Zhang, J. Jiang, *J. Phys. Chem. B* **2005**, *109*, 14011.

[44] J. B. Ran, H. Zeng, J. Cai, P. Jiang, P. Yan, L. Y. Zheng, Y. Bai, X. Y. Shen, B. Shi, H. Tong, *Chem. Eng. J.* **2018**, *333*, 20.

[45] J. Zhuang, C. H. Kuo, L. Y. Chou, D. Y. Liu, E. Weerapana, C. K. Tsung, *ACS Nano* **2014**, *8*, 2812.